POLITECNICO
DI TORINO

Automotive vibration oriented design of a 100kW integrated liquid cooled wireless power transfer system

Supervisor: Professor GUGLIELMI PAOLO

Student Name: Yao Fuxing
Student Number: s242583

Abstracts

Nowadays, the significance of electrical vehicle has raised dramatically in the background of the depletion of fossil fuel resources. However, the charging technology is still in the development period, especially the wireless power transfer technology. Currently, there are merely a small number of EVs equipped with ultra-fast charging system, and none of them apply the water cooling technology, which has substantially high cooling efficiency. The ASSURED project in Europe has launched a new project to provide a charging solution for Fiat Doblo electrical version, concerning the cooling technology.

In this paper, we mainly focus on the newly design of the water cooling system for this 100 kW ultra-fast wireless power transfer system, with its vibration oriented mechanism design applying machine design techniques to guarantee its fixture stability during the travel of vehicle. Besides, we also consider that this cooling system also must cool down the battery.

In the beginning, we make an approximate estimation on the loss generated on the WPT and the battery. Following this estimation, we calculate the parameter needed for the cooling system. Subsequently, we use both SimulationX and Solidworks to simulate and verify the designed cooling system, using temperature as the criteria. Finally, the fixture method is chosen and verified.

Keywords

Electrical vehicle, Wireless power transfer, Ultra-fast charging, Water cooling

Contents

1. Introduction: The cooling system and vibration oriented mechanism of the wireless power transfer system on electric vehicle

1.1 The wireless power transfer system on electric vehicles

1.1.1 Background

It is an internationally recognized effective strategy to develop electric vehicles for mitigating energy shortages and environmental pollution, which is crucial for the future of the world. Take China's oil consumption as an example. In 2009, net oil imports amounted to about 204 million tons, and the import dependency reached 52%, far exceeding the international call-out standard of 35%. Among them, vehicle fuel consumption accounts for 1/3 of total oil consumption. Therefore, the development and promotion of alternative fuels for automobiles and electric vehicles to reduce fuel consumption has important strategic significance for alleviating environmental pollution, ensuring energy security and supply, and the country's sustainable development. Due to the advantages of zero emissions, relatively mature technology, and economical efficiency, pure electric vehicles powered by batteries have become environmentally friendly models which has been encouraged by governments of all countries and vigorously developed by various automobile manufacturers. However, due to the limitation of power battery capacity, the current driving range of EVs is relatively short. The construction of battery charging stations has become the biggest bottleneck restricting the application and development of EVs[1]. To this end, all countries are vigorously building charging stations to promote the application of EVs, such as the United States, plans to build 8 million charging stations; Japan plans to build 1,000

charging stations in Tokyo in 2012, and so on.

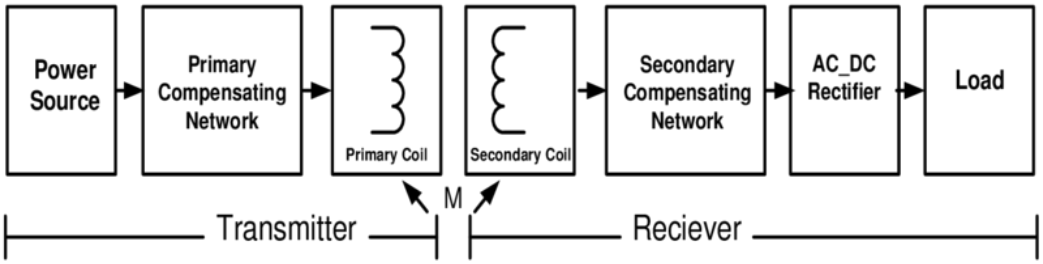

Figure 1. 1 Block Diagram of Inductive Link Wireless Power Transfer System

Power battery electric charging methods include contact charging and wireless charging. The contact charging adopts the metal contact of the plug and the socket to conduct electricity; the wireless charging or the wireless power transmission (WPT) realizes the power transmission through the electromagnetic field. For WPTs for EVs, transformer's primary and secondary windings are placed outside the vehicle and inside the vehicle respectively, and electrical energy is transmitted through the coupling of high-frequency magnetic fields. Compared with contact charging, WPT is easy to use, as well as safe, no spark and electric shock, no dust and contact loss, no mechanical wear and corresponding maintenance problems, and can adapt to a variety of harsh environments and weather. WPT facilitates unattended automatic charging and mobile charging. Under the premise of ensuring the required mileage, frequent charging can significantly reduce the power battery capacity of the EV, reduce the weight of the vehicle body, and increase the effective utilization of energy. Reducing the power battery capacity, the initial purchase cost of EVs can be reduced, and the marketization of EVs can be promoted. The huge demand for EV's WPT and the unlimited business opportunities contained therein have made the development and application of related technologies quite active.

Types of WPT	Induction Coupling	Resonant Coupling	Microwave Power Transfer
Transmitted Power Source	Electromagnetic Induction	Electromagnetic Resonance	Microwave, Radio wave and Laser
Transmitter	Few turns of copper coil	Few turns of primary coil with small gaps and secondary coil 10 times of turnings as in the primary coil without gap	Transmitting Antenna with a wave guide
Receiver	Few turns of copper coil	Few turns of copper coil	Rectenna with SCR
No. of Receivers get into	Single receiver is possible	Multi receiver is applicable	Single receiver
Direction flow of power	EMI on the same axis (max. 25% misalignment)	Omni directional power transfer	Single direction (need line of sight for transmission)
Complexity	Low	Medium	High
Efficiency	Low	High	High
Radiation Power	Non-radiant energy	Non-radiant energy	Radiant energy
Frequency Range	110 – 205 kHz	6.78MHz for power transfer and 2.4GHz for control signals	300MHz – 300GHz
Safety	Harmless	Possible danger of sparks produced at several million volts	Harmful to human beings such as telecommunications
Distance	5mm distance	Maximum 1km distance achieved (But Tesla himself achieved up to 42km)	50mm
Loss during Transmission	High	Medium	Low
Power Wave	Continuous	Oscillated power signal (Sparks)	Continuous

Table 1. 1 Comparison on various types on wireless power transmission techniques

For instance, typical applications include the 30kW passenger electric transporter at the National Geothermal Park in New Zealand, multiple WPT-EV models from GM, Nissan and Toyota, the WPT mobile charging trial highway in Los Angeles, USA, and the BMW 7 series equipped with an automotive WPT mobile phone charger sold in Korea. Car and so on. Although WPT has a number of advantages mentioned above, its low efficiency and high heat generation problems compared to contact power supply restrict its application, and it also poses challenges for R&D personnel. The charging host movement of the electric vehicle contains a high-power conversion circuit. The high-power conversion circuit is often implemented using a half-bridge or full-bridge circuit structure. Switching electronic devices such as IGBTs or MOSFETs are generally used as the bridge circuit structure in the main switching device. Switch-type electronic devices that are actually used are not ideal switches. They have a saturation voltage drop when turned on, and switching power consumption is generated during switching. Therefore, conduction losses and switching losses are generated, which are collectively referred to as device losses. The loss value of

the device is proportional to the current flowing in the switch-type electronic device, so the greater the output power of the high-power conversion circuit, the greater the current value and the greater the device loss. Device losses generally translate into device heating, so the greater the device losses, the greater the heat generated. At the same time, the electromagnetic induction charging coil will also produce about 5%-10% power loss. For the coil, there are several parameters that are more important and have a greater impact on power loss: quality factor, own turbine losses, and DC internal resistance.

1.1.2 Standards and products

The development of new energy vehicles is hindered by battery cost and cruising range to a certain extent, so wireless charging is regarded as one of the useful solutions to promote the development of new energy vehicles[2]. The American Society of Automotive Engineers (SAE) released the wireless charging standard SAE TIR J2954 on May 31, 2016. It is a technical guideline for the charging of pure electric vehicles (EVs) and plug-in hybrid electric vehicles (PHEVs) using wireless power (WPT) technology and has been considered as a wireless charging standard for electric vehicles[3]. The release of the wireless charging guide will definitely help vehicle manufacturers speed up the

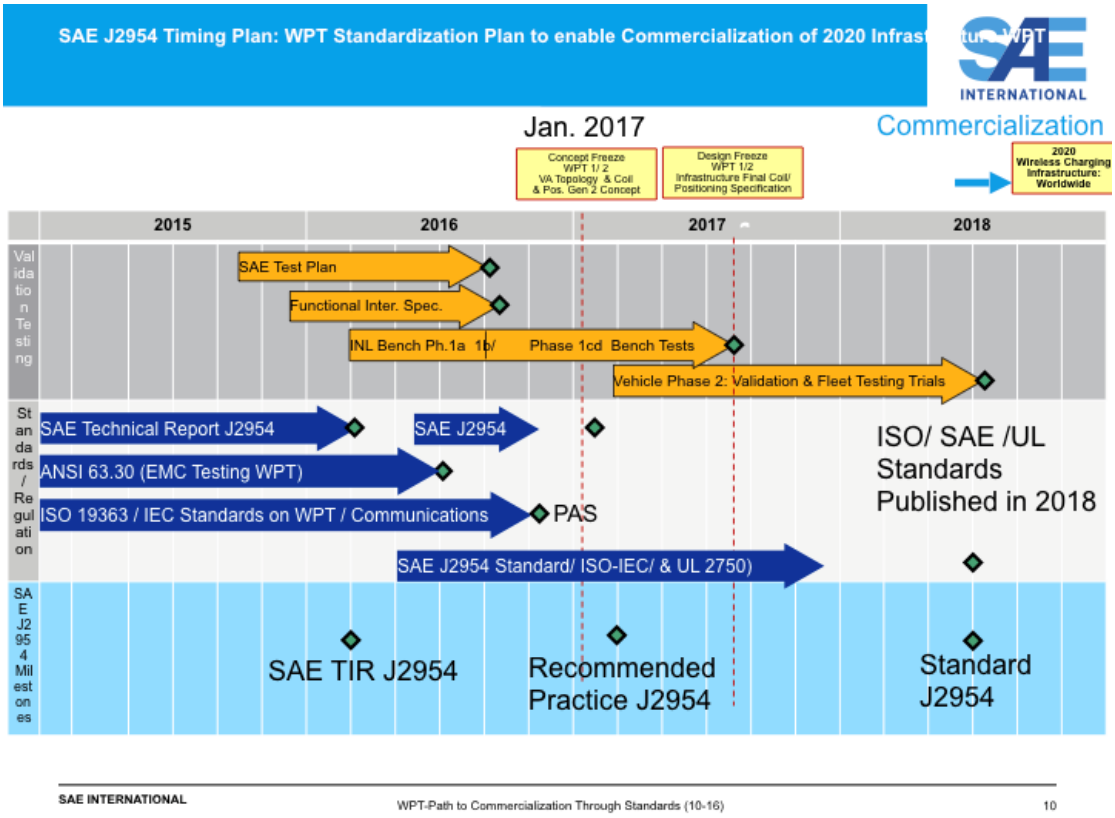

Figure 1. 2 SAE J2954 timing plan

development of related innovations for EVs and PHEVs and other new energy vehicles, thus boosting the development of wireless charging on the supply side for vehicles.

Standardization is necessary for commercialization of high power wireless power transfer (WPT) of PH/EVs, since wireless charging has rapidly become the mainstream for consumer electronic devices in low power applications. In order to achieve a basis for the start of commercialization for WPT, it is important to define criteria for safety and electromagnetic limits, efficiency and interoperability targets, as well as a test setup for the acceptance of WPT, all of which is addressed in SAE TIR J2954.

SAE International Wireless Power Group Chairman Jesse Schneider said, "The use of SAE TIR J2954 wireless power transmission will change the PH/EV new energy car game rules. A series of documents will help consumers to quickly park their vehicles with TIR J2954 equipment in the parking area, you don't need to do anything to walk away. The PH/EV hybrid will charge itself."

The Wireless Charging Guide determines the wireless charging frequency band and four different charging speeds. Among them, the general frequency is 85kHz frequency band (81.39k-90kHz); The four kinds of charging speeds are as follows: First, the ordinary charging output power of passenger cars is set at 3.7kW (WPT 1); Second, public taxis and other multiplication the general charge output power of the vehicle is set at 7.7 kW (WPT 2). Third, the fast charge output power in Europe is represented as 11 kW (WPT 3). Fourth, the fast charge output power in other regions is set at 22 kW (WPT 4) etc.

	WPT Power Class			
	WPT1	WPT2	WPT3	WPT4
Maximum input Volt Amps	3.7kVA	7.7kVA	11.1kVA	22kVA
Minimum target efficiency	>85%	>85%	>85%	TBD
Minimum target efficiency at offset position	>80%	>80%	>80%	TBD

WPT power classifications for L.D. vehicles

Z-Class	VA Coil ground clearance range (mm)
Z1	100 – 150
Z2	140 – 210
Z3	170– 250

Offset direction	Value (mm)
ΔX	±75
ΔY	±100
ΔZ	Z_{nom}-Δ_{low} -> Z_{nom} +Δ_{high}

Figure 1. 3 Standards of WPT system from SAE J2954 TIR

In July 2016, Qualcomm announced that it had signed a WEVC license agreement with Lear, a supplier of car seats and electrical systems. Lear will incorporate Qualcomm Halo

electric vehicle wireless charging technology in its product portfolio[4] to support plug-in hybrid and pure electric vehicle manufacturers and wireless charging infrastructure companies[5] to commercialize WEVC systems. In accordance with the terms of the agreement, Qualcomm granted Lear to develop, manufacture and provide paid patent licenses for the WEVC system based on Halo technology. Qualcomm will mainly provide professional knowledge and technical support in the future[6].

Qualcomm's Halo electric car wireless charging technology has been authorized for use by three suppliers: Lear, Ricardo and Brusa Elektronik. In addition to Qualcomm, WiTricity, KAIST, Momentum Dynamics, and Evatran currently offer wireless charging technology for electric vehicles. Although the majority of companies have their own intellectual property in the field of EV wireless charging technology, only Qualcomm and WiTricity have begun licensing their technology to third-party hardware vendors.

At present, 29 automotive companies support the J2954 charging guidelines, including 11 OEMs such as GM, Ford and Toyota, 4 commercial vehicles, and 14 parts and components companies. The standardization of wireless charging technology is only the first step to promote wireless charging. Next, we need to solve the compatibility problem of each car system. In 2018, SAE will publish international standards that ensure compatibility with other company systems.

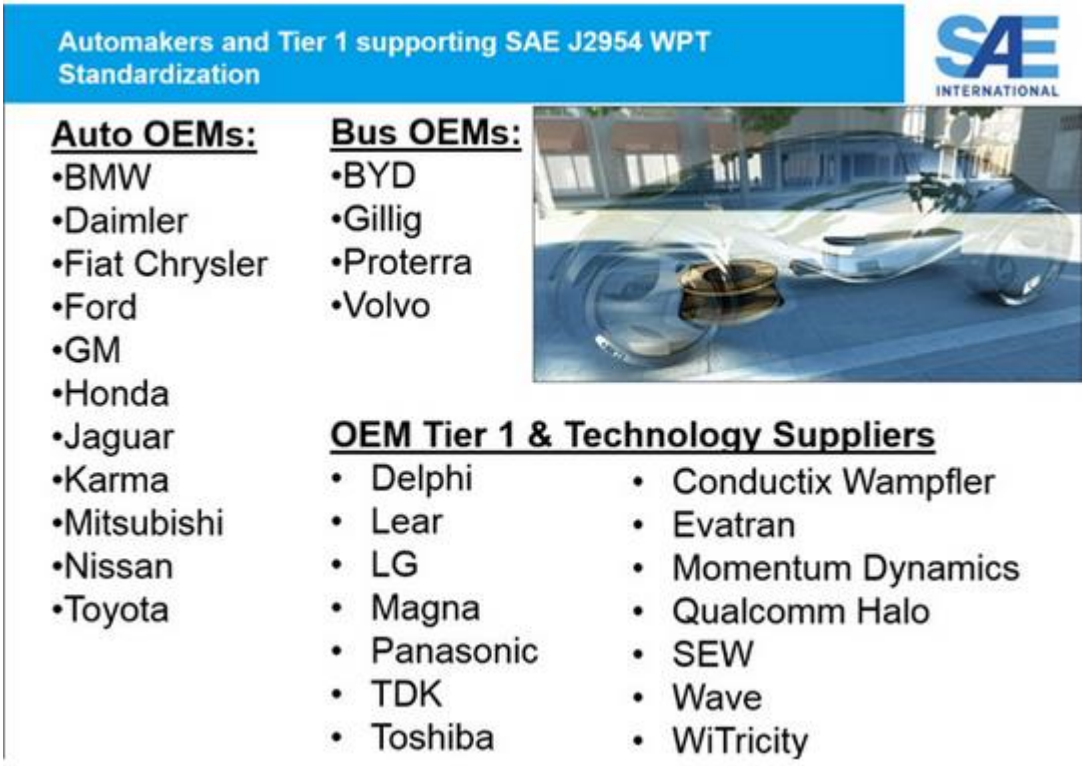

Figure 1. 4 Automakers and Tier 1 supporting SAE J2954 WPT standardization[7]

1.2 The cooling system of the wireless power transfer system on electric vehicles:

The excessively high temperature caused by the huge heat generated by the wireless power transfer system may cause the components to withstand excessive expansion thermal stress, resulting in the destruction of the components and structures, thereby reducing the lifetime of the components until failure. More than 55% of electronic device failures are caused by excessive temperatures. As the temperature continues to rise, the failure rate of various components in electronic equipment also shows a sharp increase in an exponential way, which will inevitably reduce the reliability of electronic equipment. It has become a key issue to solve the problem of heat dissipation in wireless charging circuits and other electronic devices to ensure its normal operation, and it is also a key issue studied by current scholars.

The efficient cooling system can quickly transfer heat to the outside environment. At present, the cooling methods are mainly air-cooling, and the technology of liquid-cooling has not been realized yet. Air cooling is the most widely used heat dissipation technology, because it has the advantages of stable operation, easy installation, and low cost, and has applications in many devices. The air-cooled radiator is generally composed of two parts: a heat sink and a fan. The air is used as an intermediary to cool the objects to be cooled. Its basic principle is to force the heat dissipation by the fan to reduce the temperature of the heat sink. However, air cooling also brings problems such as high noise and violent heat dissipation. In recent years, the air-cooling has been proceeding toward a large-volume pattern, which has caused inconvenience to the installation of the radiator, and has also made the air-cooling unsuitable for the heat dissipation with high heat flux density. Therefore, liquid cooling technology has attracted increasingly attention.

Now there are several liquid cooling technologies that could be used for future wireless power transfer system. Liquid cooling technology transfers energy to the cold plate and then carries it away through the liquid flow. Compared with air cooling technology, liquid cooling technology has many advantages, such as: low noise, low vibration, high efficiency, and strong environmental adaptability. However, since the liquid cooling technology requires a separate cooling circulation system, it is much costlier than air cooling. Since water has a high specific heat capacity and thermal conductivity and a relatively low cost, water is generally used as a coolant for liquid cooling. According to the installation method of water cooling, water cooling can be divided into two situations: built-in water cooling and external water cooling. For the built-in water cooling method, it mainly consists of a radiator, a water pump, a water pipe, and sufficient cooling liquid, and requires a sufficient space inside the chassis, which makes the built-in water-cooled heat dissipation system have a relatively large “volume”. As for the external water-cooling method, the heat dissipating

water tank, the water pump and the water pipe are all arranged outside the chassis, which can not only reduce the occupied space of the internal space of the chassis, but also can obtain better heat dissipation effect. The application of external water-cooling heat dissipation methods in electrical equipment is very extensive, and it is also common in thermal analysis of multi-layer heat sources.

In the liquid cooling system, the most important part is the radiator, because the performance of the radiator directly determines the cooling effect of the entire cooling system. According to the structure of the flow path of the radiator, the heat sink can generally be divided into a fin type (slab) type radiator, a parallel channel radiator, and a series channel radiator.

(1) Fin (slice) type radiator: It can be divided into two types: fork fin (sheet) radiator and splay (sheet) radiator. The feature of this structure is that the fins (pieces) are added to the heat sink to increase the heat dissipation area of the heat sink, increase the degree of turbulence when the fluid flows, and achieve the purpose of enhancing the heat dissipation effect, and at the same time, the length of the straight channel can be reduced and the fluid flow rate can be increased. The literature has analyzed and studied the heat dissipation performance of the radiators in the cross-row structure and in the row structure as well as the pressure loss in the radiator. It was concluded that the overall heat transfer performance of the cross-row structure is about 20% higher, compared with the row structure. The heat change coefficient is on average 5% higher, while the fluid flow resistance is on average 50% higher.

(2) Parallel channel radiator: The parallel channel radiator is a combination of multiple channels connected in parallel, which is like the parallel electrical circuit. The variation of the flow velocity of the fluid in the parallel passage radiator is fairly uneven, and in some cases, the flow velocity of the fluid in different flow passages can be significantly different. It is due to the phenomenon that uneven distribution of temperature occurs in the heat radiators of the parallel passages, which may lead to the occurrence of uneven temperature distribution of the heat dissipating objects, thereby greatly reducing the heat radiation capacity of the parallel passages. The cooling effect of the common parallel structure is worse than that of the series structure, but the pressure loss in the parallel structure channel is smaller than in the series structure.

(3) Series channel radiators: The serial channel radiator has only one flow path in the entire flow channel structure. In the case of the same flow at the inlet, the flow rate of the fluid in the series channel is larger than the flow rate of the fluid in other structures, its convection heat transfer coefficient is also relatively large, so the heat dissipation performance of the structure is better[8]. However, the flow rate of the fluid and the convection heat transfer coefficient are not in a linear relationship. Therefore, it is obviously not feasible to simply enhance the heat transfer effect by increasing the fluid velocity. In addition, compared to

the parallel channel radiator, there is no uneven distribution of the flow velocity of the fluid in the serial channel radiator, in other words, the fluid velocity in the radiator of the serial channel is relatively evenly distributed. It is because the series channel radiator has a very good and uniform distribution of the fluid flow velocity, so its application in the industry is very extensive. In the straight portion of the series channel, the pressure loss is smaller because of the smaller pressure gradient. However, there is a large pressure gradient at the corner of the channel, although the radiator in the series channel breaks the hydraulic boundary layer and the thermal boundary layer at the corner, and this will result in the increase of convection heat transfer coefficient of the radiator at the corner[9]. But it also leads to a relatively large pressure loss at the corners of the channel. In addition, due to violent collisions between the fluid molecules at the corners of the channels, it will inevitably result in the loss of part of the energy, thus increasing the extra power for heat dissipation. Therefore, when designing a series channel radiator, it is necessary to reduce the pressure loss in the radiator as much as possible while satisfying the premise of heat dissipation[10]. The series channel radiator can be applied to the double heat source model. Therefore, it is very important to model and optimize the heat sink. It can not only predict the temperature of the heat source, but can also provide the basis for the design of the serial channel radiator, under the premise of maximizing the heat sink cooling efficiency and reduce the pressure drop within the radiator.

The use of simulation software for thermal simulation analysis and research mainly provides the basis for the design of heat dissipation equipment. At present, most researches are using existing advanced computer-aided simulation software to perform related thermal analysis. After the temperature distribution is obtained, the cooling device is optimized.

1.3 The vibration oriented mechanism of the wireless power transfer system on electric vehicle

Due to the vibration generated by the impact of the elastic elements in the suspension system, in order to improve the ride comfort of the vehicle, a suspension is arranged in parallel with the elastic element. In order to damp the vibration, the vibration damper used in the automobile suspension system is mostly hydraulic vibration damping. The working principle of the device is that when the relative movement between the frame (or body) and the axle is caused by the vibration, the piston in the shock absorber moves up and down, and the oil in the shock absorber cavity repeatedly passes through a different cavity. The pores flow into the other cavity. At this time, the friction between the wall of the hole and the oil and the internal friction between the oil molecules form a damping force on the vibration, so that the vibration energy of the automobile is converted into the thermal energy of the oil and then is absorbed by the shock absorber to be emitted to the atmosphere.

When the cross section of the oil passage and other factors are constant, the damping force increases or decreases with the relative movement speed between the frame and the axle (or wheel), and is related to the viscosity of the oil.

The vibration of the wireless power transfer system can be reduced or offset by the suspension system on vehicle. Since the ultra-fast WPT system has a relatively large volume (850mm*850mm*75mm), and large mass (50~60kg), it is critical to ensure the stability during the travel of the vehicle. Thus, the fixation in terms of mechanical connection between WPT system and the vehicle ought to be sufficiently strong.

2. The research content

2.1 The goal of the ASSURED project

Figure 2. 1 The ASSURED project

ASSURED is mainly focus on evaluating several infrastructures in different cities across Europe, facilitating the urban commercial vehicles' electrification and their integration with high power fast charging infrastructure[11].

The project started from October 2017 with the goal of developing and testing high-power solutions for heavy-duty, full-size and urban applications. The basic goal are designed to supply energy for a great number of buses, verifying that each of these solutions will be able to charge different types of EV.

The usage of creative strategies of charging management will make great contribution to reduce the total cost of operational and ownership, air pollution, as well as the noise. Another part which will be developed is the grid stability to ensure energy supply security, which is necessary for future usage as a great number of vehicles will rely on the wireless charging infrastructure.

To achieve this, ASSURED project will test six different public transport buses, one delivery truck, one light commercial delivery vehicle and two garbage trucks, with automatic ultra-fast charging, which means that the human interaction is avoided during the charging process. The charging solutions tested by ASSURED will take into account various types of plug-in and wireless charging technologies.

The aim is to charge different types of vehicles by using the same infrastructure, which will help support the standardization of the components of the infrastructure and reduce costs if it is successful. Before this project, the test of interoperability of the charging solutions

Figure 2. 2 Electric vans in logistics and other utility vehicles

applied has not been performed.

Its main objectives are:

1. Understanding the attitudes and needs of the end-users, operators and cities when it comes to ultra- fast charging infrastructure for the next generation of electric buses, trucks and commercial vans in metropolis;

2. While reducing the environmental impact of the urban transport, especially air and noise pollution, developing and testing of the innovative charging management strategies to achieve the optimization of operational costs and ensure grid stability;

3. Providing end-users, operators and cities with scalable and interoperable high-power ultra-fast charging solutions among several main charging solution providers in Europe;

4. Evaluating and calculating the cost, noise, energy conversion efficiency, impact on the grid and environmental impact of the solutions from ASSURED;

5. By eliciting probative value and knowledge on ultra-fast charging solutions for decision-makers, facilitating the ASSURED business cases and project results across Europe.

2.2 The introduction of the Doblo electric vehicle

2.2.1 Information

In February 2010, Tofaş have revealed their development activities on the All-Electric version of their Doblo 2010.

Fiat's Tofas joint venture in Turkey is to team up with Arcelik, the country's largest appliance-maker, to develop an electric powertrain for the Doblo van. Tofas, owned 38% by Fiat, is to invest up to E20million to build the Doblo EV, reports Automotive News, with a view to production by mid-2011.

The vehicle itself was also introduced to press in July 2010, as "The First Commercial Electrical Vehicle Developed in Turkey". It has been also revealed that, Tofas will be FIAT's development pole for electric light commercial vehicles (LCV). In the one millionth ceremony of the Doblo, the Doblo EV was tested by press and Turkish Minister of Industry and Commerce, Nihat Ergün.

It has a 100KW static wireless charging system, and consists of: optimized electric van

Figure 2. 3 the Fiat Doblo electric vehicle

demonstrator with fast wireless charging system and verification of new E/E System for fast static wireless charging.

2.2.2 Cooling system

Currently, the water cooling technology has not been used for fast wireless charging system, since all of the existing WPT systems, which belongs to WPT1, 2 and 3 (according to SAE J2954 standard), apply air cooling as an economic option, because of the limit heat released from those system.

However, the Doblo's 100KW ultra-fast WPT system, which belongs to WPT4 (according to SAE J2954 standard), will create great number of heat in a short time, thus the necessity of the application of water cooling solution becomes much higher. Therefore, our goal is to design such a water cooling system to satisfy the requirement of high amount of heat transfer during charging process.

3. Loss analysis of wireless power transfer system on electric vehicle and design of its cooling system

3.1 Loss analysis of wireless power transfer system on electric vehicle

In the power conversion circuit of the wireless power transfer system of the electric vehicle, the power loss caused by the high-frequency switch operation of the power electronic device is the main source of the system loss. The power loss of power electronic devices makes the system less efficient, and even causes system damage due to increased device temperature. Abide by the law of conservation of energy when the cooling system reaches steady state of the balance of heating. That is, the energy that is generated by the loss of the power electronic device is equal to the energy dissipated in the radiator per unit time. Therefore, it has great significance for the loss analysis of the power conversion circuit of the wireless power transfer system of electric vehicle.

3.1.1 Loss analysis of the power conversion circuit

In our case, the power of wireless power transfer system of the electric vehicle is set to 100kW, the circuit structure is shown in Figure 3.1. It can be seen that the power conversion circuit mainly consists of three parts: input rectifier circuit, inverter circuit and output rectifier circuit. The input rectifier circuit consists of six diodes, while the inverter circuit consists of four IGBTs, and the output rectifier circuit consists of four fast recovery diodes[12]. Its working principle is that the input rectifier circuit rectifies and filters the three-phase AC power supply into DC power, the inverter circuit converts the DC power into high-frequency AC power to the primary coil, after the secondary coil receives the high-frequency AC power of the primary coil, the output rectifier circuit AC power rectifies and filters the high-frequency AC power into DC power supply to charge the battery pack[13][14][15].

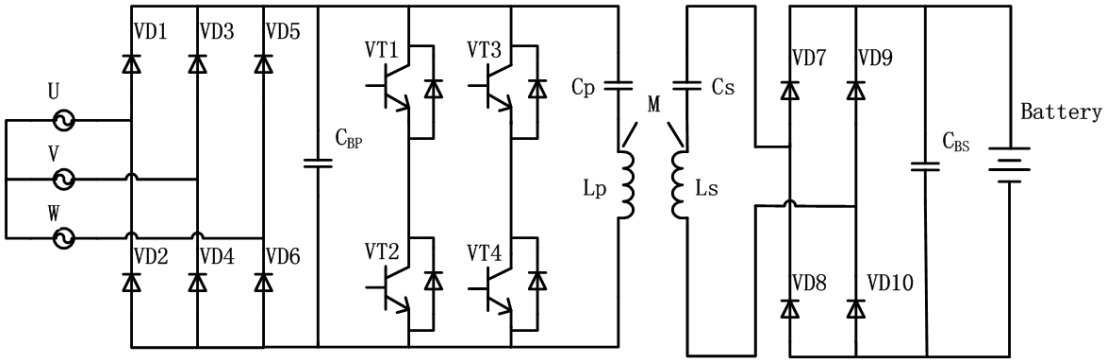

Figure 3. 1 The circuit of wireless power transfer system of electric vehicle

The following describes the loss analysis of the input rectifier circuit, inverter circuit and output rectifier circuit of the 100kW wireless power transfer system of electric vehicle. It can be seen from the above that the power electronic device in the system are mainly composed of rectifier diodes and IGBTs. Therefore, we mainly focus on the loss of diode and IGBT.

1. Loss analysis of diode

The losses of diode mainly include the following: turn-on loss, on-state loss, recovery loss, and turn-off loss, where the diode turn-on and turn-off losses are negligible.

1-a. The on-state loss of diode

From the approximate linearization of the output characteristic curve of the diode, a linear relationship between the voltage across the diode and the current flowing through it can yielded:

$$U_{VDF} = U_{VDF} + R_{VDF} \cdot I_C$$

Where:

U_{VDF} is the forward voltage drop of diode, U_0 is the threshold voltage, R_{VDF} is the on-state

equivalent resistance of diode, I_C is the on-state current of diode.

Then, when the diode is turned on, the above voltage and current are integrated to obtain the conduction loss of the diode in one conduction period, that is the on-state loss[16]:

$$P_{VD-C} = \int U(t) \cdot I(t) \cdot F(t) dt$$

Where:
U(t) is the forward voltage drop of diode, I(t) is the On-state current of diode, F(t) is the time function of diode, when the diode is turned on, we define F(t)=1, and when the diode is turned on, we define F(t)=0[17].

In addition, the loss of the on-state of the anti-parallel diode of the IGBT is:

$$P_{VD-C} = \left(\frac{1}{2\pi} - \frac{cos\,\varphi}{8}\right) \cdot U_{VDF} \cdot I_C + \left(\frac{1}{8} - \frac{cos\,\varphi}{3\pi}\right) \cdot R_{VDF} \cdot {I_C}^2$$

Where:
φ is the phase angle of voltage and current, U_{VDF} is the forward voltage drop of diode, R_{VDF} is the On-state equivalent resistance of diode, I_C is the On-state current of diode. The on-state equivalent resistance can be obtained from the manufacturer.

1-b. The switching loss of diode

According to the characteristics of the diode and the operating characteristics of the circuit, its turn-on losses can be ignored, and we only consider its turn-off loss. The sum of energy consumed by a single shutdown can be calculated using the manufacturer's database. When the switching frequency is f_s, the calculation formula of the turn-off loss of diode is:

$$P_{VD-S} = f_S \cdot \sum_{n=1}^{f_S} E_{VD-OFF}$$

Where:
$E_{VD\text{-}OFF}$ is the energy that the diode turns off once at a certain current.

After the above formula is linearized, the switching loss expression of diode can be obtained as:

$$P_{VD-S} = E_{VD-OFF} \cdot \frac{f_S \cdot U_{DC} \cdot I_O}{\pi \cdot U_N \cdot I_N}$$

Where:
U_N and I_N are the nominal voltage and nominal current of the diode, U_{DC} is the amplitude of the DC voltage, and I_O is the amplitude of output current.

2. Loss analysis of IGBT

The losses of IGBT mainly include turn-on loss, on-state loss, turn-off loss, driving loss, and off-state leakage loss. The turn-on losses and turn-off losses are collectively referred to as switching losses and refer to the loss of IGBT during turn-on and turn-off. Switching loss is the main source of the loss of IGBT, and with the increase of switching frequency, the proportion of total IGBT losses gradually increases, which has become a major factor affecting the efficiency of the wireless power transfer systems of electric vehicles. The on-state loss refers to the loss due to the voltage drop of IGBT's conduction state. The driving loss refers to the power loss by IGBT during the switching process of the control pole and the power loss to maintain a certain driving current during the conduction process. In general, the driving loss can be ignored compared with other losses. The off-state leakage loss refers to the off-state power loss that may be caused by a tiny leakage current when the IGBT is turned off. However, due to the very small leakage current, the power loss is between several tens of microamperes and several hundred microamperes, its loss power is very low and negligible.

2-a. The on-state loss of IGBT

In the wireless power transfer system designed, the single IGBT in the inverter circuit only passes the positive half cycle or negative half cycle current, and its on-state loss calculation equation is[17]:

$$P_{IGBT-C} = f_S \cdot \int_0^T U_{CE}(t) \cdot I_C(t) \cdot F(t)dt$$

Where:

$U_{CE}(t)$ is the voltage of IGBT between the collector and emitter, $I_C(t)$ is the current across collector, F(t) is the time function of IGBT, when the IGBT is turned on, we define F(t)=1, when the diode is turned on, we define F(t)=0. $U_{CE}(t)$, $I_C(t)$ and F(t) are all the functions of time t. T is the period, f_s is the switching frequency, and f_s=1/T.

The $U_{CE}(t)$ and $I_C(t)$ of the IGBT fluctuate with time, and the output characteristic curve representing the relationship between the two is nonlinear. In order to obtain a relation that is easy to calculate, the output characteristic curve is approximately linearized to obtain a linear relationship between the $U_{CE}(t)$ and $I_C(t)$ of IGBT:

$$U_{CE}(t) = U_0 + R_{CE} \cdot I_C(t)$$

Where:

In the above formula: U_0 is the threshold voltage of the IGBT, and R_{CE} is the equivalent resistance between the collector and the emitter when the IGBT is turned on.

In our inverter circuit, it can be deduced that the IGBT's on-state loss expression is as follows:

$$P_{IGBT-C} = \left(\frac{1}{2\pi} + \frac{cos\,\varphi}{8}\right) \cdot U_0 \cdot I_{C-MAX} + \left(\frac{1}{8} + \frac{cos\,\varphi}{3\pi}\right) \cdot R_{CE} \cdot {I_{C-MAX}}^2$$

Where:

In the above formula: φ is the phase angle of voltage and current, U_0 is the threshold voltage of the IGBT, $I_{C\text{-}MAX}$ is the maximum current across collector, R_{CE} is on-state equivalent resistance. The on-state equivalent resistance can be obtained through the U_{CE}-I_C curve provided by the manufacturer[18].

2-b. The switching loss of IGBT

When the switching frequency is f_s, the calculation formula of the switching loss of IGBT is:

$$P_{IGBT-S} = f_S \cdot \sum_{n=1}^{f_S} (E_{IGBT-ON} + E_{IGBT-OFF})$$

Where:

In the above formula: $E_{IGBT\text{-}ON}$ is the energy that the IGBT turns on once at a certain current, $E_{IGBT\text{-}OFF}$ is the energy that the IGBT turns off one time at a certain current. f_s is the switching frequency.

The quantitative relationship between the energy of the IGBT turn-on and turn-off losses and the I_C can be obtained from the manufacturer's database. This relationship is nonlinear therefore, similar linearization is needed to facilitate calculations, then the switching loss expression of a single IGBT after linearization is:

$$P_{IGBT-S} = \frac{f_S}{\pi} \cdot (E_{IGBT-ON} + E_{IGBT-OFF}) \cdot \frac{U_{DC}}{U_{CE-N}} \cdot \frac{I_{C-MAX}}{I_{C-N}}$$

Where:

$E_{IGBT\text{-}ON}$ is the energy that the IGBT turns on one time under the nominal voltage and nominal current conditions, $E_{IGBT\text{-}OFF}$ is the energy that the IGBT turns off one time under the nominal voltage and nominal current conditions, $U_{CE\text{-}N}$ and $I_{C\text{-}N}$ are the nominal voltage and nominal current of the IGBT, U_{DC} is the amplitude of the DC voltage, and $I_{C\text{-}MAX}$ is the maximum current across collector.

Based on the above analysis, the expression for the total loss of a single diode is[19]:

$$P_{VD} = P_{VD-C} + P_{VD-S}$$

And the expression for the total loss of a single IGBT is:

$$P_{IGBT} = P_{IGBT-C} + P_{IGBT-S}$$

The anti-parallel diode is integrated inside the IGBT used in the inverter circuit, so the total loss is:

$$P_{IGBT-TOTAL} = P_{VD} + P_{IGBT}$$

Therefore, for the 100kW wireless power transfer system of electric vehicle designed in this paper, the Infineon's DDB6U180N16RR_B11 module is used as the diode of the input rectifier circuit, in the condition of I_{FVD}=150A and V_{FVD} = 1.2V, the RFVD can be calculated as 8mΩ. The Infineon's FF300R12KS4 module is used as the IGBT of the inverter circuit, which conduction voltage drop is V_{CE}=3.2V. The Infineon's ND242S10K as the diode of the output rectifier circuit, in the condition of I_{FVD}=800A and V_{FV}=1.55V, the R_{FVD}= 1.94mΩ. By consulting the database provided by the manufacturer of the diode and IGBT used, it can be calculated:
The total loss of the input rectifier circuit P_{IN}= 676W.
The total loss of the inverter circuit is P_{CON}=905W.
The total loss of the output rectifier circuit is P_{OUT} = 563W.

3. Loss analysis of other devices

In the wireless power transfer system of the electric vehicle designed, the primary coil and the secondary coil are matched with a resonant compensation capacitor[20]. For the loss of the resonant compensation capacitor, its series equivalent resistance can be directly measured with an impedance analysis equipment, and then its loss can be estimated based on the actual current across during operation. The series equivalent resistances of the primary and secondary resonant compensation capacitors are R_{CP-SER}=10mΩ, R_{CS-SER}=10mΩ, respectively. In actual operation, the currents in the primary and secondary coils are approximately 250A and 200A, respectively. Therefore, it can be estimated that the losses of the primary and secondary resonant compensation capacitors are 625 W and 400 W, respectively.

3.1.2 Loss analysis of the coil

The coil loss of the wireless power transfer system of the electric vehicle mainly includes the copper loss of the coil wire and the hysteresis loss of the magnetic shielding material. The copper loss refers to the loss caused by the resistance of the coil wire, when the high-frequency current passes through the coil, the equivalent resistance increases, so that the loss on the coil also increases. The hysteresis loss is mainly due to the hysteresis effect of the magnetic shielding material used.

1. The loss analysis of copper

The equivalent circuit model of the coil part of the wireless power transfer system of the electric vehicle designed in this paper is shown in Figure 3.2. U_{IN} is a high-frequency AC

voltage source, L_P and L_S are the inductances of the primary coil and the secondary coil respectively[21], C_P and C_S are the resonant compensation capacitances of the primary coil and the secondary coil respectively, M is the mutual inductance between the primary coil and the secondary coil, R_P and R_S are the equivalent resistance of the primary coil and the secondary coil respectively, and R_L is the load[22].

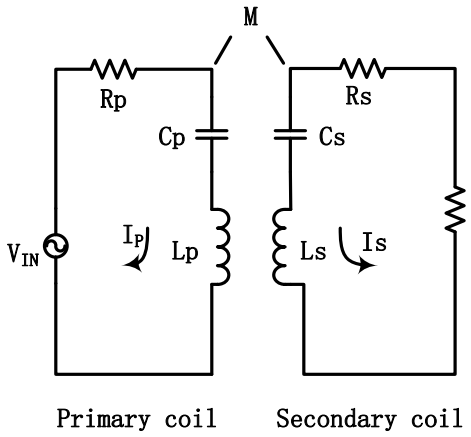

Figure 3. 2 Equivalent circuit model of the coil part

When the power supply U_{IN} is sinusoidal and the angular frequency is ω, according to the Kirchhoff voltage law[23], the KVL equations is listed for the primary coil and the secondary coil circuit[24].

$$\left(j\omega L_P + \frac{1}{j\omega C_P} + R_P\right) \cdot \dot{I_P} + j\omega M \dot{I_S} = \dot{U_{IN}}$$

$$j\omega M \dot{I_P} + \left(j\omega L_S + \frac{1}{j\omega C_S} + R_S + R_L\right) \cdot \dot{I_S} = 0$$

Assuming that Z_P is the impedance of the primary coil, Z_S is the impedance the secondary coil, then the following equations can be obtained[25]:

$$j\omega L_P + \frac{1}{j\omega C_P} + R_P = Z_P$$

$$j\omega L_S + \frac{1}{j\omega C_S} + R_S + R_L = Z_S$$

Thus, it can calculate from the above two equations[26]:

$$\dot{U_{IN}} = \left(Z_P + \frac{(\omega M)^2}{Z_S}\right) \cdot \dot{I_P}$$

Then, it can be easily calculated that the input active power P_{IN}, output active power P_{out}, and the efficiency η of the wireless power transfer system are as follows:

$$P_{in} = I_P \cdot [R_P + Re \cdot \frac{(\omega M)^2}{Z_S}]$$

$$P_{out} = \left(\frac{\omega M U_{IN}}{Z_P \cdot Z_S + (\omega M)^2}\right)^2 \cdot R_L$$

$$\eta = \frac{P_{out}}{P_{in}}$$

When the wireless power transfer system works in resonance, the system has the maximum wireless transmission efficiency η_{MAX}.

$$\omega = \frac{1}{\sqrt{L_P \cdot C_P}} = \frac{1}{\sqrt{L_S \cdot C_S}}$$

$$\eta_{MAX} = \frac{(\omega M)^2 \cdot R_L}{[R_P \cdot (R_S + R_L) + (\omega M)^2] \cdot (R_S + R_L)}$$

As can be seen from the above equation, the mainly factors influencing the efficiency of the wireless power transfer system are the mutual inductance M, the angular frequency ω, the resistance values of the primary coil and the secondary coil R_P, R_S and the load R_L[27].

We define the quality factor of the primary coil as Q_P, it can be calculated[28]:

$$Q_P = \frac{\omega L_P}{R_P}$$

We define the quality factor of the secondary coil as Q_s, it can be calculated[28]:

$$Q_S = \frac{\omega L_S}{R_S}$$

We define the coupling coefficient of the primary coil and secondary coil as k, it can be calculated:

$$k = \frac{1}{\sqrt{L_P \cdot L_S}}$$

Then, the system efficiency can be expressed as Q_P, Q_S, and k as follows:

$$\eta = \frac{k^2 \cdot Q_P \cdot Q_S}{\left(\sqrt{k^2 \cdot Q_P \cdot Q_S + 1} + 1\right)^2}$$

It can be seen from the above equation that the efficiency of the wireless power transfer system increases with the coupling coefficient k and the quality factor Q_P and Q_S, of the primary coil and the secondary coil. Then, the method of improving the efficiency of the

wireless power transfer system can be started from two aspects. One is to increase the coupling coefficient k between the coils, and the other is to increase the quality factor Q_P and Q_S of the coils.

Therefore, for the 100kW wireless power transfer system of electric vehicle designed in this paper, the internal resistance of the coil is known to be R_P=14mΩ and R_S=14mΩ, respectively. In practice, the currents in the primary coil and the secondary coil are approximately 250 A and 200 A, respectively. It can be calculated that:

The loss of primary coil is P_{COIL-P}=875 W

The loss of secondary coil is P_{COIL-S}=560.5 W.

2. The loss analysis of magnetic shielding material

Assume a magnetic material has a cross-sectional area of A, an average magnetic path length of L, and a number of coil turns of N, if the voltage U(t), the current is I(t), the magnetization curve is shown in Figure 3.3[29]. In the figure: B_m is the saturation flux density, Br is the residual flux density, H_c is the coercive force, S_A is the area of the magnetic material from $-B_r$ to B_m and the area surrounded by the vertical axis, S_B is the magnetic material from B_m to B_r. The area enclosed by the curve and the vertical axis, the slope of the curve represents the relative permeability μ.

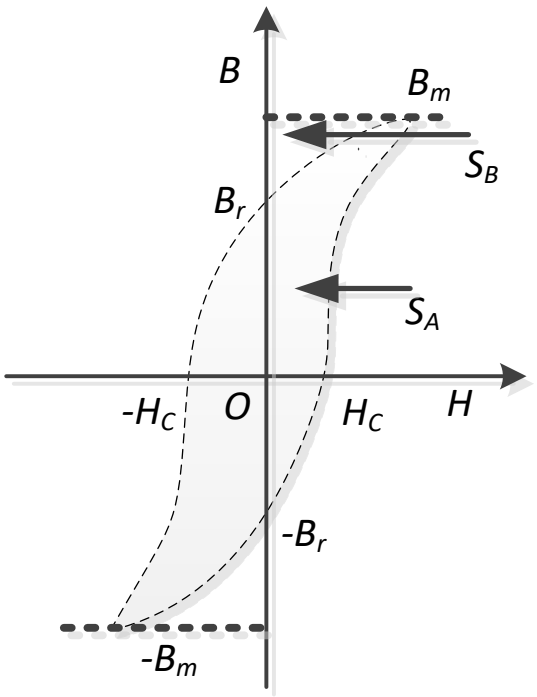

Figure 3. 3 The magnetization curve of magnetic material

According to ampere loop law:

$$H = \frac{I(t) \cdot N}{L}$$

And according to the law of electromagnetic induction:

$$u = N \cdot \frac{d\phi}{dt} = N \cdot A \cdot \frac{dB}{dt}$$

In half a cycle, the energy entering the magnetic shielding material is[30]:

$$\int_0^{\frac{T}{2}} U(t) \cdot I(t) dt = \int_{-B_r}^{B_r} N \cdot A \cdot \frac{dB}{dt} \cdot \frac{H \cdot L}{N} dt = V \int_{-B_r}^{B_r} HdB$$

$$= V\left(\int_{-B_r}^{B_s} HdB - \int_{-B_s}^{B_r} HdB\right) = V \cdot (S_A - S_B)$$

Where V=AL is the core volume.

From the above equation, it can be seen that the energy loss of the magnetized core material in the half cycle is $V(S_A\text{-}S_B)$, which is the area enclosed by the magnetization curve $-B_r\text{-}B_m\text{-}B_r$ and the vertical axis. Similarly, the magnetization core loss in the other half cycle is the area enclosed by the magnetization curve and the vertical axis in the second and third quadrants, that is, the area enclosed by the hysteresis loop represents the hysteresis loss of the unit volume core[31]. When the magnetic core has a certain volume, each cycle of magnetization consumes energy proportional to the encircled area of the hysteresis loop. The higher the frequency, the greater the power loss. The larger the magnetic induction swing, the greater the area of envelopment and the greater the loss[32].

Hysteresis loop depends on the characteristics of the magnetic material, from the above analysis we can see that in order to reduce the hysteresis loss in the magnetic core should make the hysteresis loop enclosed area as small as possible. When B_m is constant, the higher the relative permeability μ, the smaller the area of the corresponding hysteresis loop; the lower the relative permeability μ, the larger the area of the corresponding hysteresis loop. The smaller the coercive force H_c and the residual magnetic flux density Br, the corresponding hysteresis loop becomes narrower. That is, from the perspective of selecting a magnetic material, the initial magnetic permeability μ_i is required to be high, the coercive force H_c and the residual magnetic flux density Br are smaller, that is, the corresponding hysteresis loop is of a thin high type, and the hysteresis loss is small. At the same time, the saturation flux B_m cannot be too small, otherwise it will easily affect the system operation due to the saturation of the magnetic core.

In addition, the following formula is commonly used in engineering calculations to calculate the hysteresis loss:

$$P_h = C_0 \cdot f \cdot B^2$$

Where C_0 is a constant of change depending on the material properties.

We can find that in the case of a weak magnetic field, the area enclosed by the hysteresis loop is very small, so the hysteresis loss is also very small. As the magnetic field strength increases, the hysteresis loss will increase rapidly. When the ferromagnetic material is in a strong alternating magnetic field, hysteresis loss occurs due to hysteresis effect. M_n-Z_n ferrite has very low electrical conductivity and high relative magnetic permeability. At low frequency, the losses in the magnetic core are almost all hysteresis losses.

The assuming operating frequency of the wireless power transfer system in our case is 85Khz, so the hysteresis loss is the dominant loss in the system magnetic piece. Because the hysteresis loss is also proportional to the magnetic core volume, in addition to the magnetic materials used in the thin and high hysteresis loop, the magnetic core should be designed to minimize the volume of the magnetic core to reduce hysteresis loss in the magnetic core. The parameters of M_n-Z_n ferrite are shown in Table 3.1[33].

Magnetic shielding material	Conductivity（S/m）	Relative Magnetic permeability
M_n-Z_n ferrite	1	2200

Table 3. 1 The parameters of Mn-Zn ferrite

The loss on the coil was measured under the conditions of only the coil, and the conditions of both coil and the magnetic shielding material. The measured values were subtracted to obtain loss of the magnetic shielding material. For the loss, the fitting curve expression for the loss of the magnetic shielding material is: $F(x)=0.0187x^2$, which can be seen in the same form as the formula[34].

Therefore, for the 100kW wireless power transfer system of electric vehicle designed in this paper, it can be calculated that:
The loss of magnetic shielding material for the primary coil is $P_{MSM\text{-}P}$=360.5W.
The loss of magnetic shielding material for the secondary coil is $P_{MSM\text{-}S}$=525W.

3.1.3 Loss analysis of the battery

The heat generation mechanism of a lithium battery mainly refers to the thermal behavior caused by various electrochemical reactions inside the battery and the ohm resistance generated by the physical resistance of lithium ions to each constituent material. In addition, the chemical reactions occurring at the electrodes will also cause polarization internal resistance, which will produce tolerance polarization internal resistance in the process of lithium ion transfer. These are collectively referred to as polarization internal resistance, in

which tolerance internal resistance and current magnitude. The solid phase diffusion coefficient is related to the liquid phase diffusion coefficient. The study found that there are four main sources of heat for lithium battery: reaction heat Q_R, polarization heat Q_P, Joule heat Q_J, and side reaction heat Q_S. In general, the total heat generated by the battery is[35]:

$$Q_{TOTAL} = Q_R + Q_P + Q_J + Q_S$$

Where:
Q_R is the heat generated by the reversible reaction inside the battery, Q_P is the heat generated by the battery polarization reaction, Q_J is the heat generated by the battery internal resistance, and Q_S is the heat generated by the battery side reaction and self-discharge.

1. The heat of reaction: Q_R

The electrochemical reactions occurring inside the battery are reversible, lithium ions are embedded or unembedded between the positive and negative electrodes, and heat is generated during this process. The battery absorbs heat when charging, and the reaction heat is negative. The battery emits heat when discharged and the reaction heat is positive. The formula for the heat of reaction is summarized as:

$$Q_R = \frac{mnql}{MF}$$

Where:
q is the total heat generated by the positive and negative electrodes during electrochemical reaction inside the cell, F is the Faraday constant, and its value is 96484.5C/mol. I is the current during charge and discharge, n is the number of cells, and m is electrode mass, M is molar mass.

2. The heat of polarized: Q_P

Lithium battery has polarization resistance during charge and discharge. Ohm polarization, differential polarization, and electrochemical polarization usually cause polarization resistance. When the current passes through the inside of the battery, the internal resistance of the polarization will also cause a certain pressure to drop and generate heat. The formula for the polarization reaction heat is as follows:

$$Q_P = I^2 \cdot R_P = I^2 \cdot (R_0 + R_N + R_D)$$

Where:
I is the current when the battery is charged and discharged, R_P is the internal resistance of the battery, R_0 is the internal resistance of ohm polarization, R_N is the concentration of internal resistance, R_D is the internal resistance of electrochemical polarization[36].

3. The joule heat: Q_J

Lithium battery have resistors such as poles, electrolytes, and separators. When charging

and discharging, the current passes through these places, and the Joule effect generates a certain amount of heat, which is called joule heating. joule heating is positive during charging and discharging processes and is the most important source of battery heat power. The calculation formula is:

$$Q_J = I^2 \cdot R_J$$

Where:
I is the current during charging and discharging, R_J is the ohm resistance of the cell.

4. The heat of side effects: Q_S

Lithium battery will undergo side reactions under over-charge and over-discharge conditions. Decomposition of electrode materials caused by self-discharge of batteries and decomposition of electrolytes under high temperature conditions will generate a certain amount of heat. These heats are collectively referred to as side reaction heat. However, the heat generated by self-discharge and electrolyte decomposition is small and can be ignored. The heat of side reactions is mainly heat generated under overcharge and over-discharge conditions.

Studies have shown that after the temperature of a lithium-ion battery reaches 75℃, the heat of reaction Q_R begins to increase sharply and becomes the main source of heat generation; at temperatures below 75℃, the reaction heat is not significant, relative joule heat and polarization heat. The proportion of reaction heat is very small, only about 1%. A battery pack with a reasonable thermal management system has a battery operating temperature much less than 75℃, so the heat of reaction can be ignored during calculation. In addition, the heat generated by the side-reaction heat Q_S compared to the other three parts is also very small and can be neglected in the calculation[37].

The joule heat Q_J and the polarization heat Q_P are positive at the time of charge and discharge, and the reaction heat Q_R is negative at the time of charge and positive at the time of the discharge, the heat generation rate of the battery in the discharge phase is higher than that of the charge phase. The heat generation rate in the medium is so large that the temperature when the battery is discharged under the same environment is higher than the temperature at the time of charging. On the one hand, it shows that the battery has less heat accumulated in the charging process, and the temperature field is more evenly distributed. On the other hand, it also shows that if the thermal management system can meet the cooling requirements of the battery pack's high-power discharge, it can also meet the cooling requirements of the battery pack charging.

Lithium battery charging and discharging process is a reversible electrochemical reaction process that emits heat, showing a clear exothermic phenomenon. Further, the positive electrode reaction of the battery shows a relatively obvious exothermic phenomenon, and the negative electrode reaction of the battery shows a weak endothermic phenomenon,

but the overall reaction of the battery shows a clear exothermic phenomenon.

Based on the above analysis, the total heat generated by the battery can be expressed as:

$$Q_{TOTAL} = Q_P + Q_J = I^2 \cdot R = I^2 \cdot (R_P + R_J)$$

Where:
R is the total battery resistance. This total resistance can be considered as the sum of the ohm internal resistance R_J and the internal polarization resistance R_P.

The physical parameters of the lithium battery monomer mentioned above are shown in Table 3.2:

Monomer Voltage (V)	Capacity (Ah)	Internal resistance (mΩ)	Volume L*W*H (mm)	Monomer quality (Kg)
3.25	200	1.4	180*90*90	4.2

Table 3. 2 The physical parameters of the lithium battery monomer

Based on the above analysis and the physical parameters of the lithium battery monomer, the heat power of the lithium battery monomer under the conditions of constant rate discharge of 1/3C, 2/3C, 1C, 2C and 3C is calculated and simulated, respectively. The data of heat power obtained when the lithium battery monomer is discharged at different rates are shown in Table 3.3:

Discharge rate (C)	Discharge time (s)	The rate of heat power (W/ m^3)	Heat power (KJ)
1/3	8220	3250	52.3
2/3	4110	11085	101.6
1	2740	26768	150.5
2	1370	48655	198.9
3	913.33	82334	247.6

Table 3. 3 The data of heat power under different rate discharge

Through the above analysis and calculation, it can be seen that the heat power of the battery monomer under the discharge rate of 1/3 C is 52.3KJ, which is much lower than the heat generation power of 247.6 KJ under the condition of the 3C discharge rate. This shows that in the case of large-current discharge of the battery, the rate of heat and heat power will increase dramatically, and the heat dissipation demand will increase dramatically

According to the data in Table 3.3, the losses of the battery monomer and the battery pack

used in the 100kW wireless power transfer system of electric vehicle designed in this paper under different charge and discharge rates can be calculated as shown in Table 3.4.

Discharge rate（C）	Losses of battery monomer（W）	Losses of battery monomer and battery pack（W）
1/3	6.36	222.6
2/3	24.72	865.2
1	54.93	1922.55
2	145.18	5081.3
3	271.1	9488.5

Table 3. 4 Losses of battery monomer and battery pack under different charge and discharge rates

3.2 Design of the cooling system of the wireless power transfer system on electric vehicle

3.2.1 Optimized design of the cooling system

The theory of heat transfer

First of all, it is necessary to introduce the principle of heat transfer. Heat transfer is energy in transit due to a temperature difference. When a difference in temperature exists within a body or among bodies a heat transfer takes place. There are three different kinds of heat transfer processes[38]:

CONDUCTION

CONVECTION

RADIATION

1. CONDUCTION HEAT TRANSFER

When in a medium (solid or fluid at rest) there is a temperature gradient a heat transfer occurs within the medium by CONDUCTION

Physical mechanism:

-Atomic and molecular activity (interaction) with an energy transfer from the more energetic to the less energetic particles

Gases & liquids: collision and diffusion

Solids: lattice vibrations and electrons migration

-Higher temperatures are associated with higher atomic energies

FOURIER'S LAW

For one-dimensional plane wall with a temperature distribution T(x) the rate of heat transfer per unit area perpendicular to the direction of transfer (x direction) is proportional to the

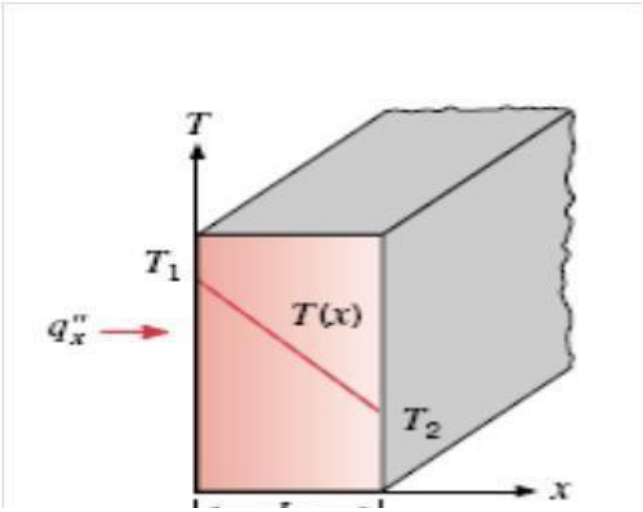

Figure 3. 4 Heat transfer through one-dimensional plane wall

temperature gradient.

$$qx'' = -k\frac{dT}{dx} \quad [W/m^2]$$

The proportionality constant is k the material thermal conductivity (W/mK)
The minus sign is due to the heat transfer direction (direction of decreasing temperatures)
At steady state, with a linear temperature distribution within the wall we have a heat flux (W/m^2):

$$\frac{dT}{dx} = \frac{T_2 - T_1}{L}$$

$$qx'' = -k \cdot \frac{T_2 - T_1}{L}$$

The heat rate equation (W) through a plane wall of area A is:

$$qx = -k \cdot A \cdot \frac{T_2 - T_1}{L}$$

2. CONVECTION HEAT TRANSFER

The heat transfer between a solid surface and a moving fluid due to a difference in temperature is called CONVECTION

Physical mechanism: is due to super imposition of two different kind of energy transfer:
-Energy transfer due to random molecular motion (conduction)
-Bulk or macroscopic motion of the fluid

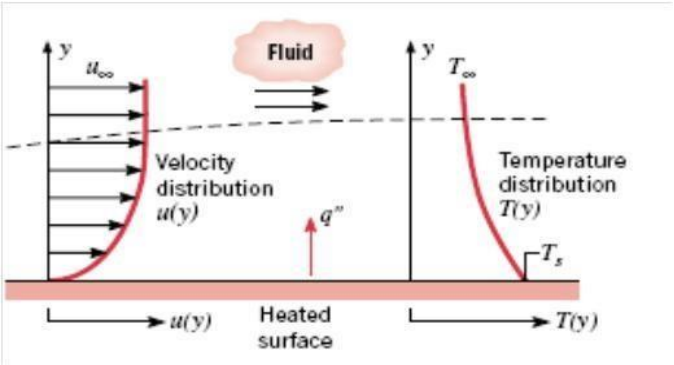

Figure 3. 5 Temperature and velocity distribution

NEWTON'S LAW

The heat flux exchanged by convection is:

$$q'' = h \cdot (T_S - T_\infty) \quad [W/m^2]$$

where:

h is the fluid convection heat transfer coefficient (W/m^2K)

T_s is the surface temperature

T_∞ is the temperature in a zone sufficiently far from the wall where the effects related to the presence of the wall are vanished.

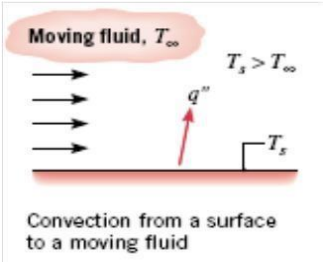

Figure 3. 6 Convection from a surface to a moving fluid

The rate of heat transfer [W] is:

$$q = h \cdot A \cdot (T_S - T_\infty) \quad [W]$$

3. RADIATION HEAT TRANSFER

The energy emitted by a surface at a certain temperature is called RADIATION

Physical mechanism: surfaces at finite temperature emit energy in the form of electromagnetic waves (photons)[39]

-The emission process may be
attributed to changes in electron configuration of the atoms and molecules

-The exchange of energy by radiation may take place also in vacuum

The rate at which energy is released per unit area (W/m) is called: emissive power

The upper limit to the emissive power (E_b=black body emissivity) is stated by the

Stefan-Boltzmann law:

$$E = \sigma \cdot T_S^4$$

Where:

σ=5.67·10-8 W/m^2K^4 is the Stefan-Boltzmann constant

T_s is the absolute temperature (K)

For a real surface:

$$E = \varepsilon \cdot \sigma \cdot T_S^4$$

where: ε is the emissivity (surface property) and 0 ≤ ε ≤ 1

4. Overall heat transfer coefficient

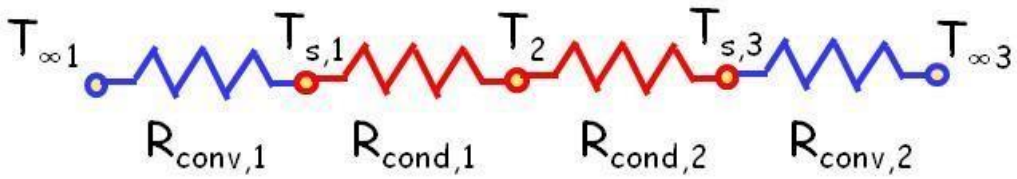

Figure 3. 7 Electrical analogy

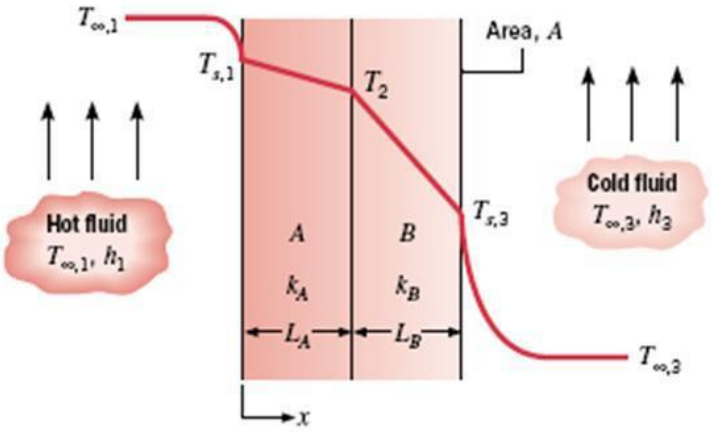

Figure 3. 8 Composite plane wall

Considering the composite wall

$$R_{tot} = \frac{1}{h_1 \cdot A} + \frac{L_A}{K_A \cdot A} + \frac{L_B}{K_B \cdot A} + \frac{1}{h_3 \cdot A}$$

$$\dot{Q} = K_r \cdot A \cdot \Delta T$$

K_r = overall heat transfer coefficient

$$K_r = \frac{1}{R_{tot} \cdot A} = \frac{1}{\frac{1}{h_1} + \frac{L_A}{K_A} + \frac{L_B}{K_B} + \frac{1}{h_3}}$$

5. Heat transfer from the coil to the coolant pipe

The coolant pipe is much more complex than a simple metal plate. Therefore, its global heat transfer coefficient K_r cannot be theoretically calculated but is experimentally

evaluated.

$$\dot{Q}_c = K_r \cdot A_r \cdot (T_{ri} - T_{ai})$$

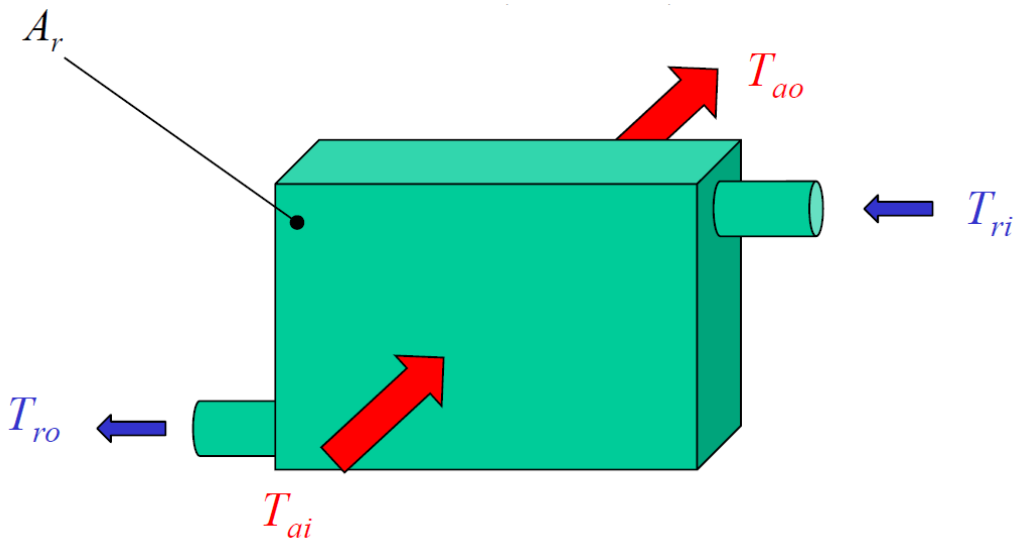

Figure 3. 9 Overall heat transfer coefficient

Where:

A_r = heat transfer area of the pipe

T_{ro} = coolant temperature at the pipe outlet

T_{ri} = coolant temperature at the pipe inlet

T_{ai} = coil temperature at the interface with pipe

6. Water flow rate to cool the coil

When the heat disposed by the WPT system is known, the coolant mass flow rate can be evaluated:

$$\dot{m}_c = \frac{\dot{Q}_c}{c_c \cdot \Delta T} = \frac{\dot{Q}_c}{c_c \cdot (T_{ri} - T_{ro})}$$

Where:

A_r = heat transfer area of the pipe

T_{ro} = coolant temperature at the pipe outlet

T_{ri} = coolant temperature at the pipe inlet

C_c = specific heat of the coolant

The designing processes

We mainly focus on the heat transfer happening between the coil which generates the heat and the pipe which contains the coolant. Thus, it is necessary to decide the global heat transfer coefficient and the minimal heat transfer area so that the dimension of the cooling pipe could be designed, as well as the minimal coolant mass flow rate.

As the information given, the coolant is set to 50% ethylene glycol solution with aluminum pipe. The coil consists of a 5mm aluminum layer, a 10mm ferrite layer and a 15mm copper-phase change material mixture (80% copper, 20% PCM in terms of mass) layer. However, the detailed information of the PCM is not given, thus we assume it as resin. Also, without knowing the specific sort of ferrite, we assume its density equals to 4000 kg/m^3, in terms of the calculation of mass. While we consider the copper-phase change material mixture as pure copper during the calculation of thermal conductivity. It is required that the coil temperature should not higher than 65°C during a 5-minute ultra-charging process, with 5kW power to be transferred.

There are also several assumptions needed to guarantee the designing phase: the coolant temperature at the inlet and outlet of the pipe are assumed to be 40°C and 45°C, respectively.

1. Estimation of the mass of coil

$$m = m_{Al} + m_{Fe} + m_{Cu} + m_{PCM}$$
$$= V_{Al} \cdot \rho_{Al} + V_{Fe} \cdot \rho_{Fe} + V_{Cu} \cdot \rho_{Cu} + V_{PCM} \cdot \rho_{PCM}$$
$$= V_{coil} \cdot (V_{Al}\% \cdot \rho_{Al} + V_{Fe}\% \cdot \rho_{Fe} + V_{Cu}\% \cdot \rho_{Cu}$$
$$+ V_{PCM}\% \cdot \rho_{PCM}) = 46.0955\ kg$$

Where[40]:
m_{Al} = mass of aluminum
m_{Fe} = mass of ferrite
m_{Cu} = mass of copper
m_{PCM} = mass of PCM
V_{Al} = volume of aluminum
V_{Fe} = volume of ferrite
V_{Cu} = volume of copper
V_{PCM} = volume of PCM
ρ_{Al} = density of aluminum
ρ_{Fe} = density of ferrite
ρ_{Cu} = density of copper
ρ_{PCM} = density of PCM

From the density database of common materials, we can easily find the density of aluminum, copper and resin are 2700 kg/m^3, 8500 kg/m^3 and 1070 kg/m^3, respectively[41].

Thus, the mass of the coil is 46.0955 kg, approximately.

2. Estimation of the heat transfer area of the coolant pipe

$$K_P = \frac{1}{\frac{L_{Al}}{K_{Al}} + \frac{L_{Cu}}{K_{Cu}} + \frac{1}{h_c}} = 1.6343 * 104 \ W/(m^2 \cdot k)$$

Where:

K_p = global heat transfer coefficient between the coil and the coolant.

H_c = convective coefficient of 50% ethylene glycol solution

K_{Al} = thermal conductivity of aluminum

K_{Cu} = thermal conductivity of copper

L_{Al} = thickness of aluminum

L_{Cu} = thickness of copper

From the table 3.4, we can find the convective coefficient of water with forced convection is 50 to 10000 w/(m^2*k). Thus, we assume the convective coefficient of 50% ethylene glycol solution equals to 1000 w/(m^2*k).

Flow type	(W/m^{2}k)
Forced convection; low speed flow of air over a surface	10
Forced convection; moderate speed flow of air over a surface	100
Forced convection; moderate speed cross- flow of air over a cylinder	200
Forced convection; moderate flow of water in a pipe	3000
Forced Convection; molten metals	2000 to 45000
Forced convection; boiling water in a pipe	50000
Forced Convection - water and liquids	**50 to 10000**
Free Convection - gases and dry vapors	5 to 37
Free Convection - water and liquids	50 to 3000
Air	10 to 100
Free convection; vertical plate in air with 30°C temperature difference	5
Boiling Water	3000 to 100000
Water flowing in tubes	500 to 1200
Condensing Water Vapor	5 to 100
Water in free convection	100 to 1200

Oil in free convection	50 to 350
Gas flow on tubes and between tubes	10 to 350

Table 3. 5 Convective coefficient of typical flow types

From the table 3.5, we can find the thermal conductivity of aluminum and copper are 220 $W \cdot m^{-1} \cdot K^{-1}$ and 390 $W \cdot m^{-1} \cdot K^{-1}$, respectively.

Material	Thermal conductivity [$W \cdot m^{-1} \cdot K^{-1}$]
Acrylic glass (Plexiglas V045i)	0.170–0.200
Alcohols, oils	0.100
Aluminium	220
Alumina	30
Copper (pure)	390
Diamond	1,000
Fiberglass or foam-glass	0.045
Polyurethane foam	0.020–0.021
Expanded polystyrene	0.033–0.046
Manganese	7.810
Water	0.591
Marble	2.070–2.940
Silica aerogel	0.020
Snow (dry)	0.050–0.250
Teflon	0.250

Table 3. 6 Thermal conductivity for common materials

Therefore, the global heat transfer coefficient equals to $1.6343*10^4$ w/(m^2*k).

$$A_P = \frac{1}{K_p \cdot (T_{coil} - T_{ci})} = 0.3198\ m^2$$

Where:

A_p = heat transfer area of the pipe

T_{coil} = temperature of the coil

T_{ci} = coolant temperature at the pipe inlet

It is easy to get that the minimum heat transfer area of pipe should be 0.2122 m^2. In our design, we set this value to 0.3198 m^2.

3. Estimation of the mass flow rate of the coolant

$$\dot{m}_c = \frac{\dot{Q}_c}{c_c \cdot (T_{ci} - T_{co})} = 0.4\ kg/s$$

Where:

T_{ci} = coolant temperature at the pipe inlet

T_{co} = coolant temperature at the pipe outlet

C_c = specific heat of the coolant

From the table 3.6, we can find the specific heat of 50% ethylene glycol solution is 3.377 $kJ \cdot kg^{-1} \cdot k^{-1}$.

	Specific Heat of Ethylene Glycol Solution *(% by volume)*							*kJ/(kg.k)*	
Temperature℃	10%	20%	30%	40%	50%	60%	70%	80%	90%
-35					3.068	2.844	2.612	2.37	
-30					3.088	2.866	2.636	2.397	
-25					3.107	2.888	2.66	2.423	2.177
-20				3.334	3.126	2.909	2.685	2.45	2.206
-15				3.351	3.145	2.931	2.709	2.477	2.235
-10			3.56	3.367	3.165	2.953	2.733	2.503	2.264
-5		3.757	3.574	3.384	3.184	2.975	2.757	2.53	2.293
0	3.937	3.769	3.589	3.401	3.203	2.997	2.782	2.556	2.322
5	3.946	3.78	3.603	3.418	3.223	3.018	2.806	2.583	2.351
10	3.954	3.792	3.617	3.435	3.242	3.04	2.83	2.61	2.38
15	3.963	3.803	3.631	3.451	3.261	3.062	2.854	2.636	2.409
20	3.972	3.815	3.645	3.468	3.281	3.084	2.878	2.663	2.438
25	3.981	3.826	3.66	3.485	3.3	3.106	2.903	2.69	2.467
30	3.989	3.838	3.674	3.502	3.319	3.127	2.927	2.716	2.496
35	3.998	3.849	3.688	3.518	3.339	3.149	2.951	2.743	2.525
40	4.007	3.861	3.702	3.535	3.358	3.171	2.975	2.77	2.554
45	4.015	3.872	3.716	3.552	**3.377**	3.193	3	2.796	2.583
50	4.024	3.884	3.73	3.569	3.396	3.215	3.024	2.823	2.612
55	4.033	3.895	3.745	3.585	3.416	3.236	3.048	2.85	2.641
60	4.042	3.907	3.759	3.602	3.435	3.258	3.072	2.876	2.67
65	4.05	3.918	3.773	3.619	3.454	3.28	3.097	2.903	2.699
70	4.059	3.93	3.787	3.636	3.474	3.302	3.121	2.929	2.728
75	4.068	3.941	3.801	3.653	3.493	3.324	3.145	2.956	2.757
80	4.077	3.953	3.816	3.669	3.512	3.345	3.169	2.983	2.786
85	4.085	3.964	3.83	3.686	3.532	3.367	3.193	3.009	2.815
90	4.094	3.976	3.844	3.703	3.551	3.389	3.218	3.036	2.844
95	4.103	3.987	3.858	3.72	3.57	3.411	3.242	3.063	2.873
100	4.112	3.999	3.872	3.736	3.59	3.433	3.266	3.089	2.902

105	4.12	4.01	3.886	3.753	3.609	3.454	3.29	3.116	2.931
110	4.129	4.022	3.901	3.77	3.628	3.476	3.315	3.143	2.96
115	4.138	4.033	3.915	3.787	3.647	3.498	3.339	3.169	2.989
120	4.147	4.045	3.929	3.804	3.667	3.52	3.363	3.196	3.018
125	4.155	4.056	3.943	3.82	3.686	3.542	3.387	3.223	3.047

Table 3. 7 Specific heat of ethylene glycol solution[42]

Therefore, the minimum mass flow rate of the 50% ethylene glycol solution equals to 0.2961 kg/s. In our design, we set this value to 0.4 kg/s.

3.2.2 Creation of the simulation model of the cooling system

1. SimulationX results

First, we use simulationX to verify whether the coolant mass flow rate (0.4 kg/s) and the heat transfer area (0.3198 m^2) we set can meet the requirement that the coil temperature should not be higher than 65°C. As the loss analysis showing, both the battery and the WPT produce 5kW heat, respectively. In order to simulate the extreme working condition, we set the initial coil temperature to 65°C. We put the battery and coil connected in a series way, setting the coil and WPT material as copper, and pipe as aluminum, to check whether the output parameter is in the range we require. The configuration is shown below:

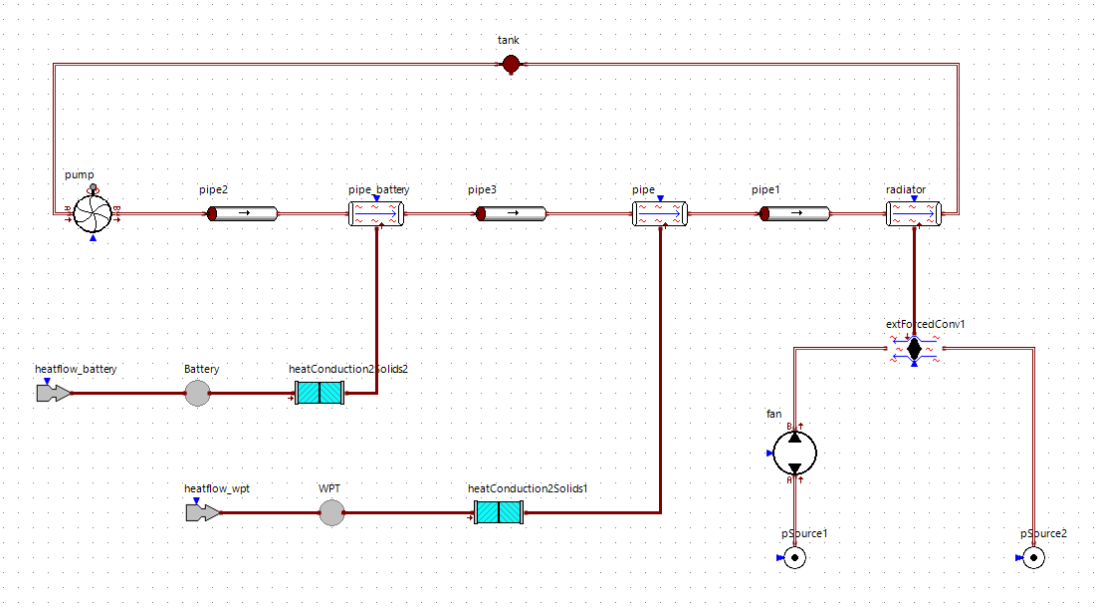

Figure 3. 10 Configuration for the cooling system of WPT

In the cooling circuit, we consider that the heat conduction happens at the interface between heat source (battery and WPT) and cooling pipe. Then the heat is transferred to the coolant by forced convection. Finally, the radiator transfers the heat from coolant to the

outside air, also by convection. For simplicity, we ignore the influence of heat radiation. Then we get the result:

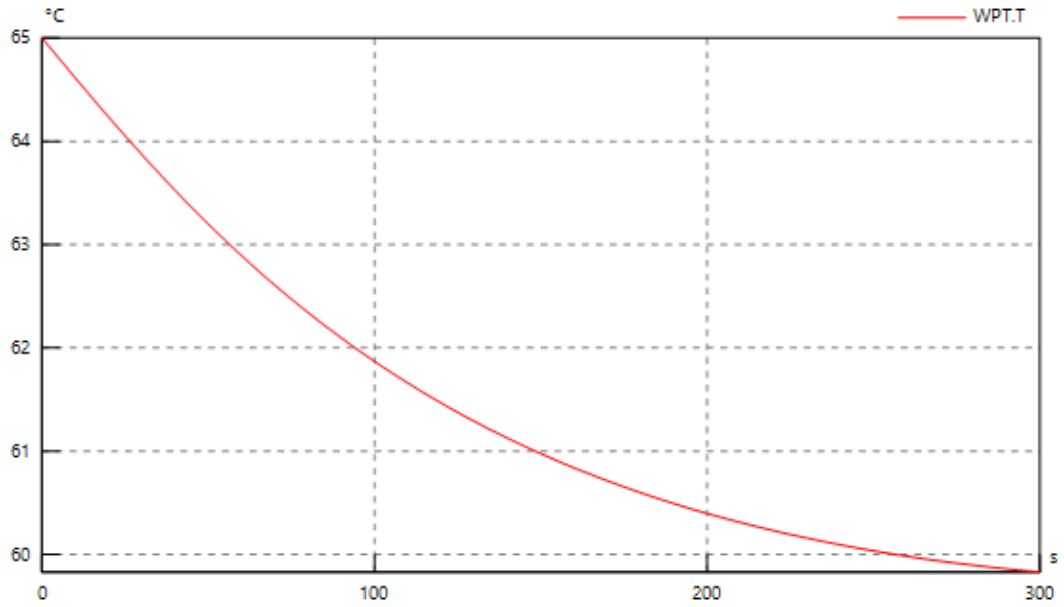

Figure 3. 11 Temperature of WPT

As shown from the figure, the temperature gradually dropped, so the coil can be cooled down by our cooling circuit.

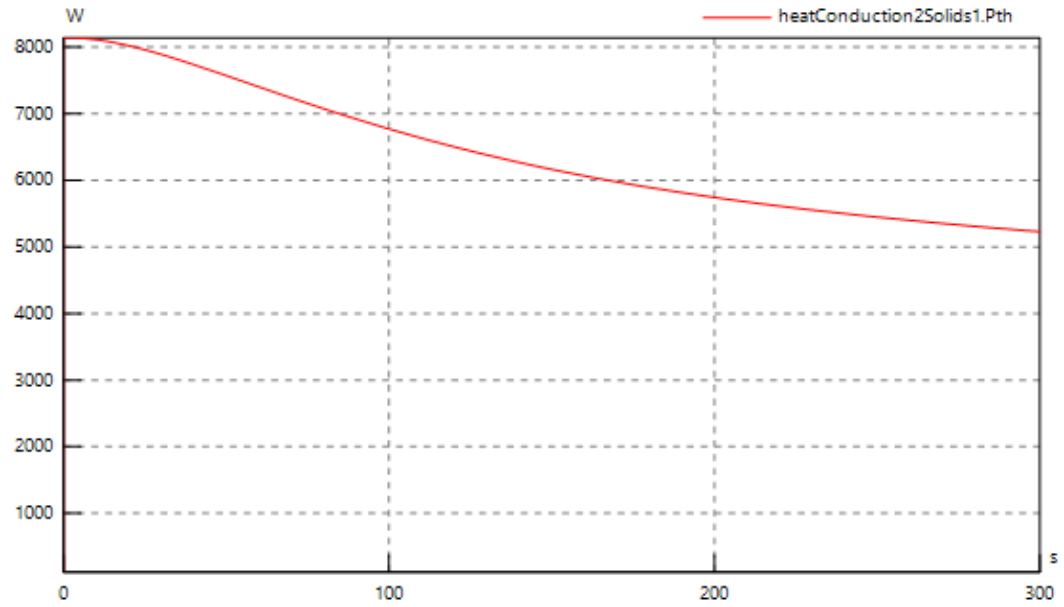

Figure 3. 12 Heat flux of WPT

The heat transfer rate between coil and the pipe reached maximum at first, then gradually drop.

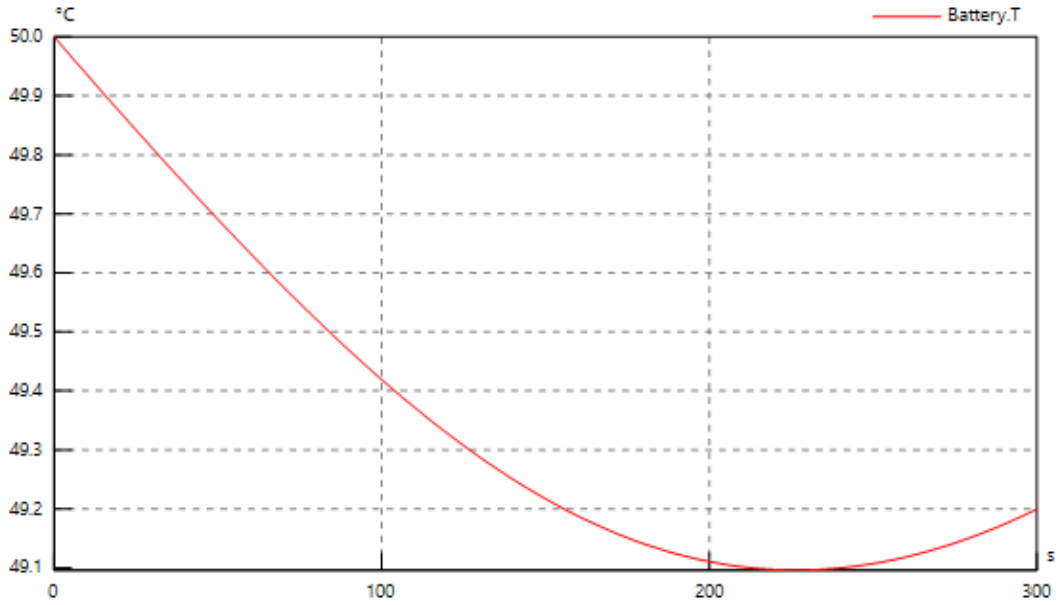

Figure 3. 13 Temperature of the battery

The trend of the temperature of battery is quite unique, which reduced at first then increase slightly. We conjecture that this phenomenon is due to the series configuration of battery and WPT.

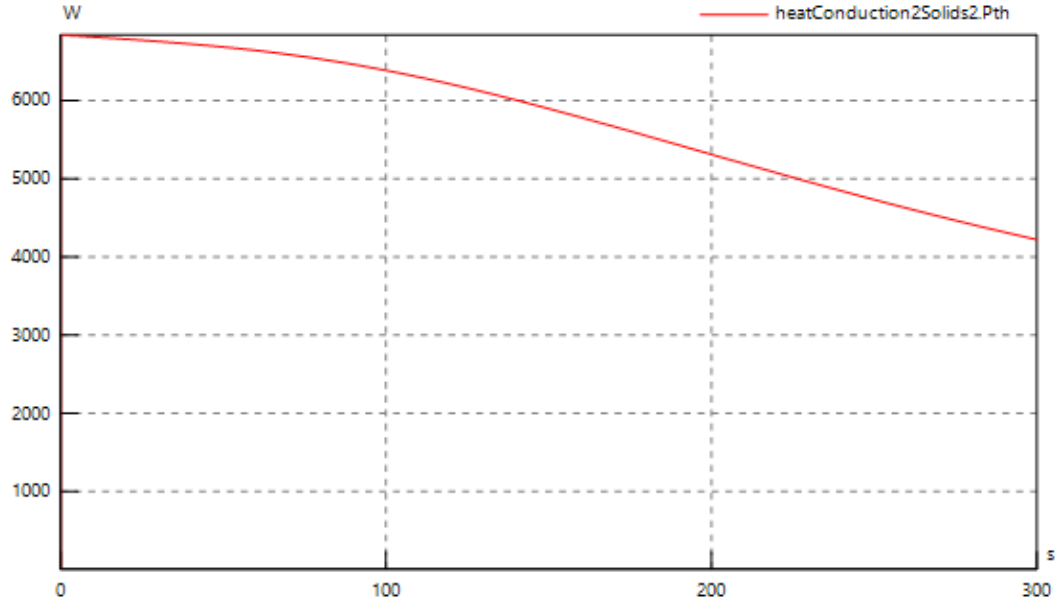

Figure 3. 14 Heat flux of the battery

The pattern of heat flux of the battery has a similar way as that of WPT, but slightly lower.

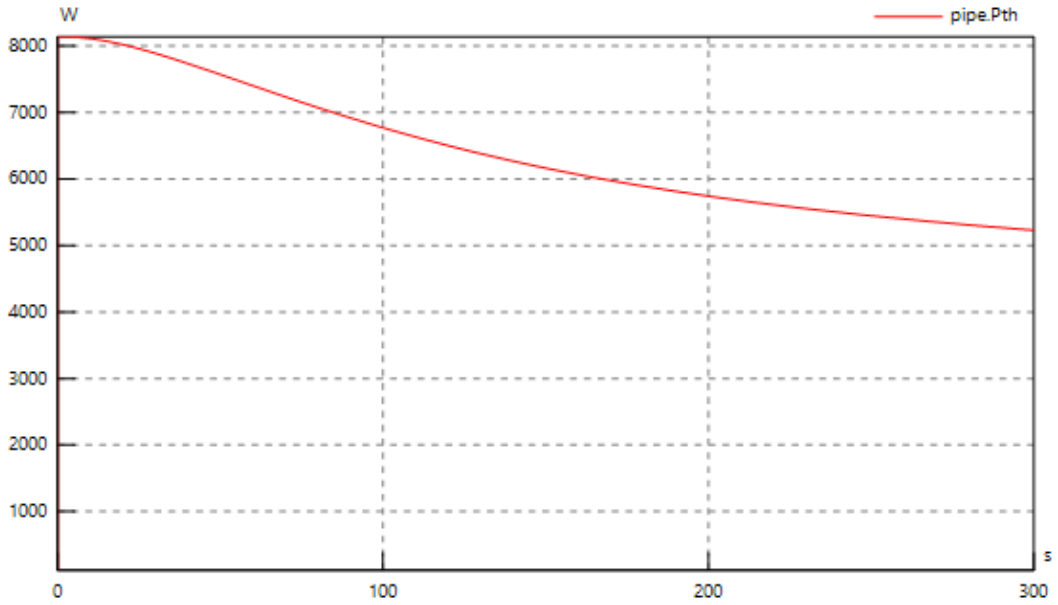

Figure 3. 15 Heat flux of the forced convection in the pipe (WPT)

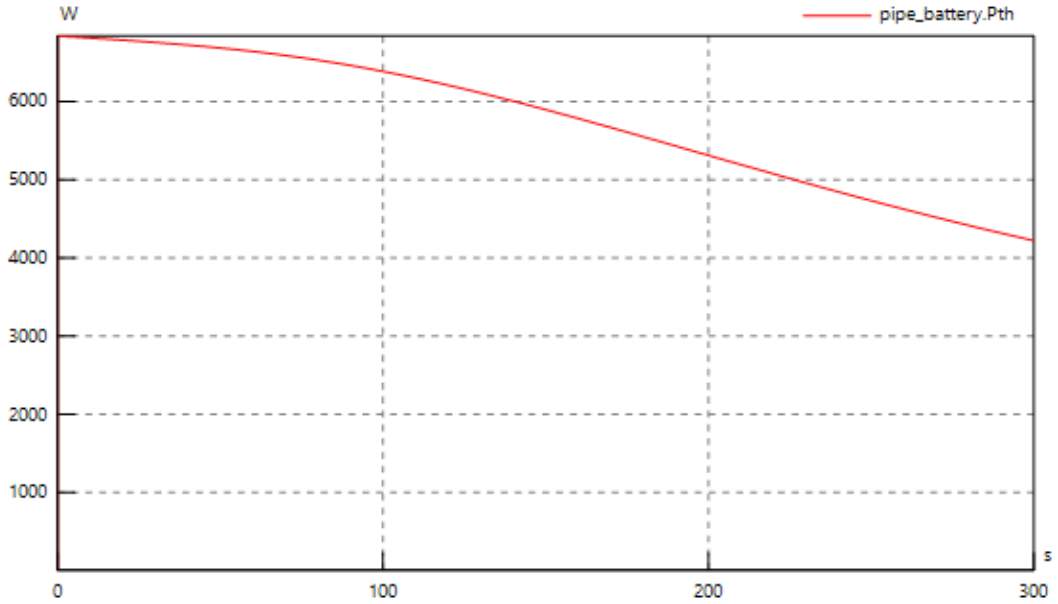

Figure 3. 16 Heat flux of the forced convection in the pipe (Battery)

The heat transfer rate of forced convection is similar as that of conduction, both for WPT and the battery.

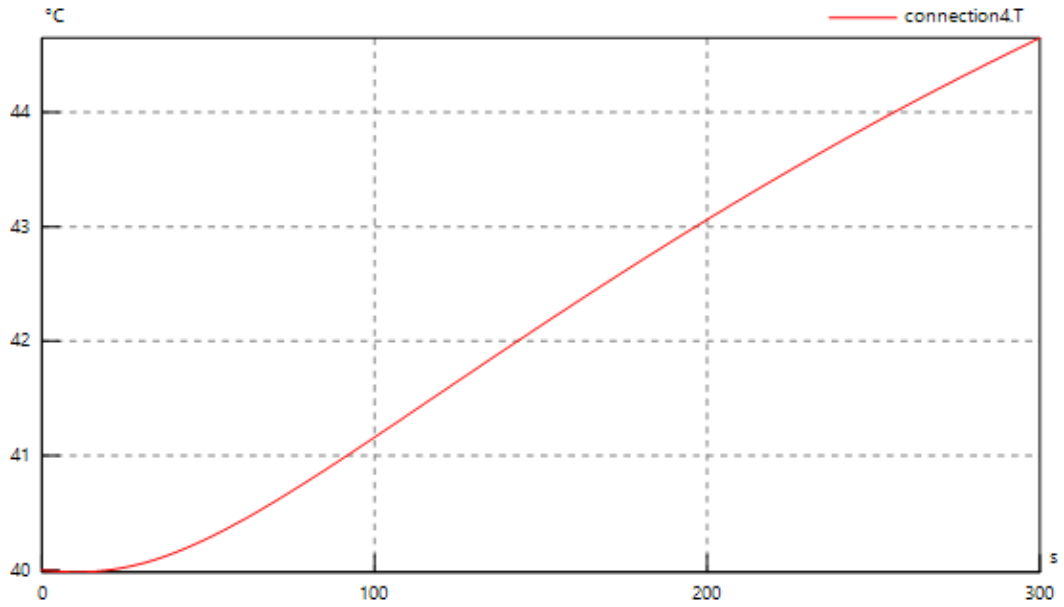

Figure 3. 17 Temperature of coolant at the outlet of the heat transfer area with WPT

We can find the coolant temperature grows significantly since it receives the heat from both WPT and the battery.

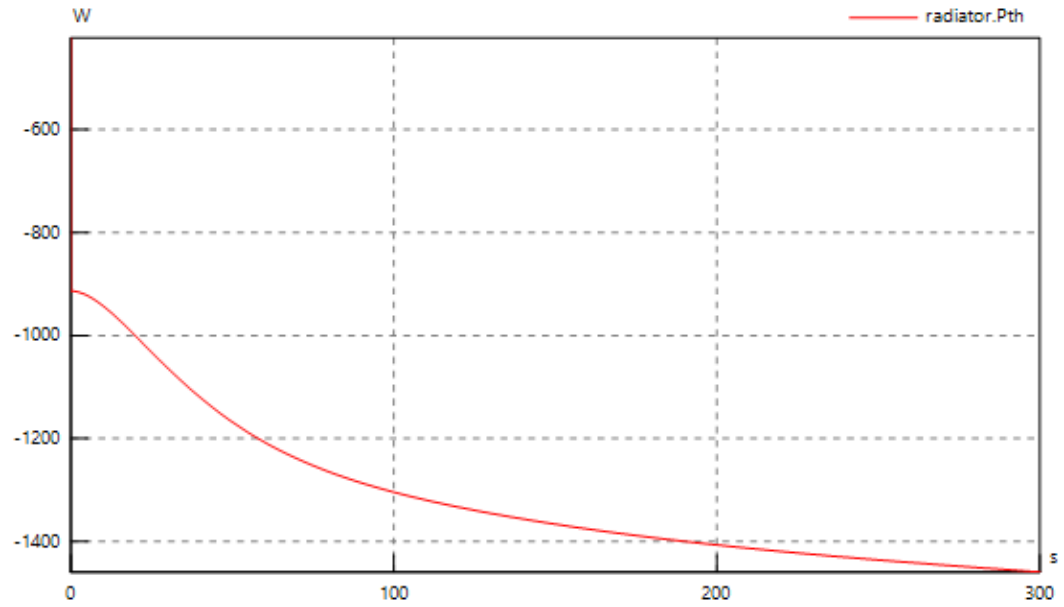

Figure 3. 18 Heat flux at the radiator

Here we can see that the value is negative since the heat is taken by the cool air at environment temperature.

2. Solidworks results

The SimulationX provides a simulation more in a theoretic way, whereas the Solidworks can illustrate a more specific one. We create a model consists of a box and the coil inside, as well as the bracket which plays a role as fixture. Due to the limit information given currently, we only draw a cooling pipe without pump, fan and radiator, as well as the components for the battery. But we can still control the mass flow rate and the heat transfer area for the WPT we design.

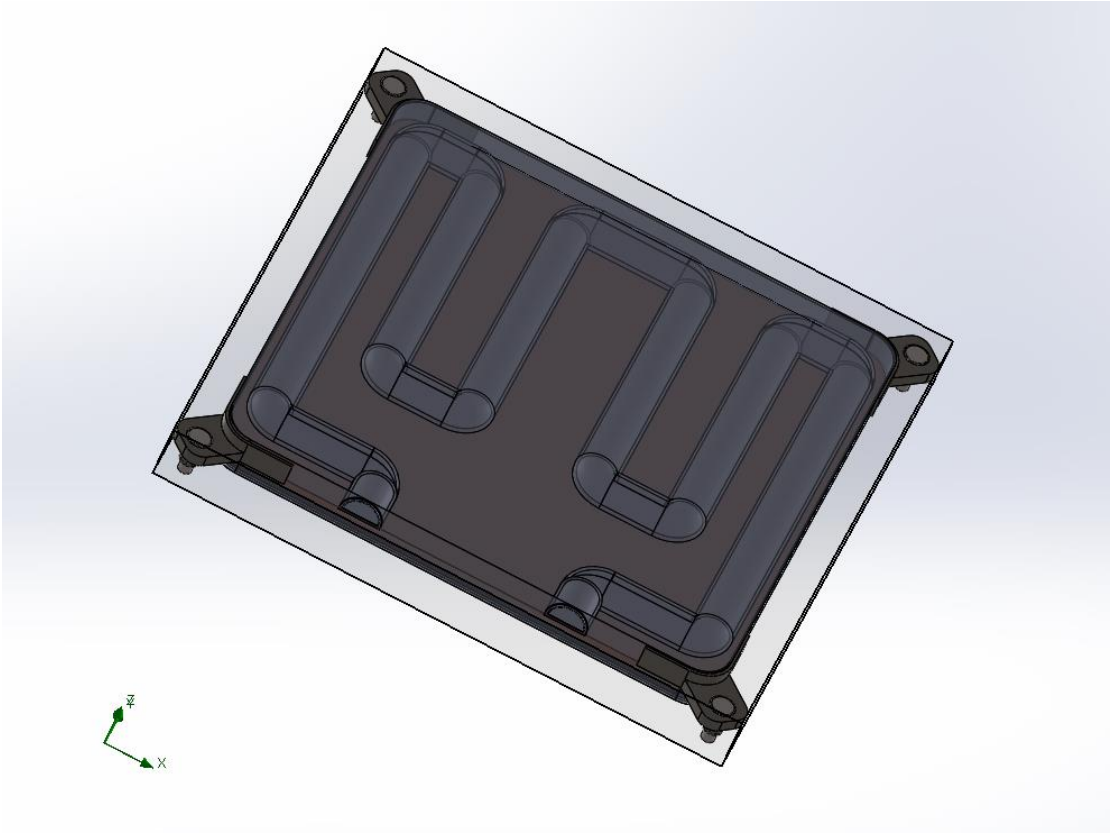

Figure 3. 19 3D model of the cooling system

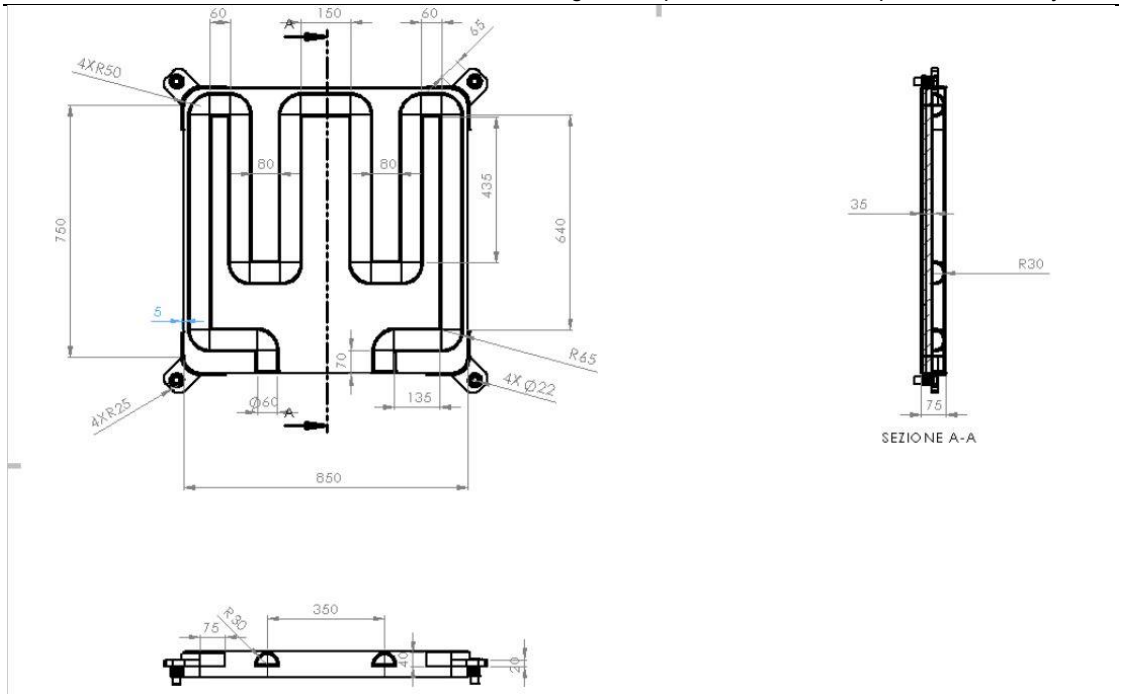

Figure 3. 20 Dimension of the cooling system

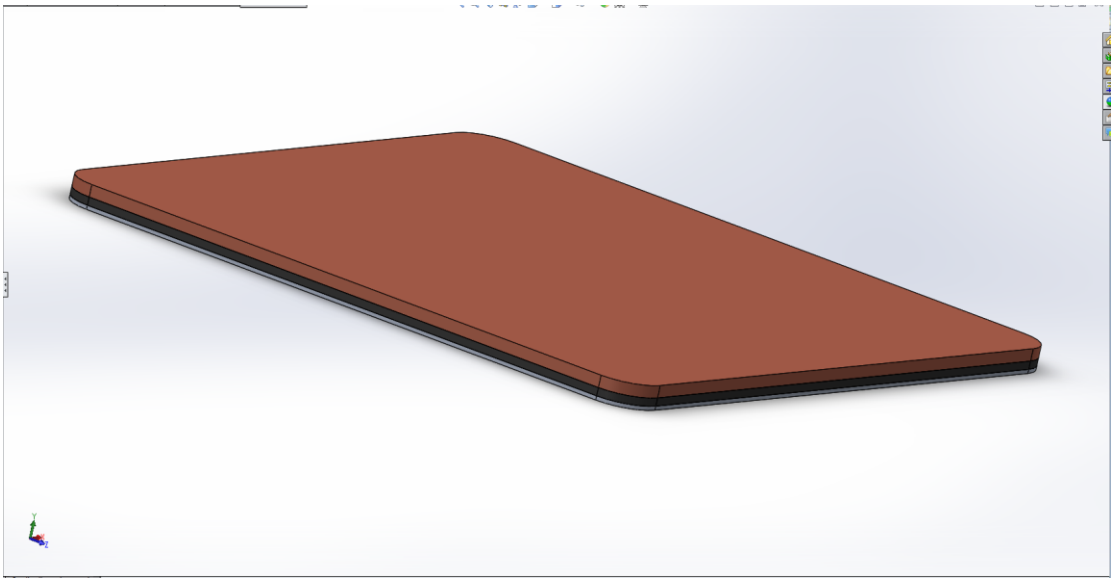

Figure 3. 21 3D model of the coil

The coil is the assembly of the three layers: aluminum, ferrite and copper. In order to simulate the extreme condition, we assume that all of the area in the box will generate heat, so we modify the shape of the coil to the same as the box.

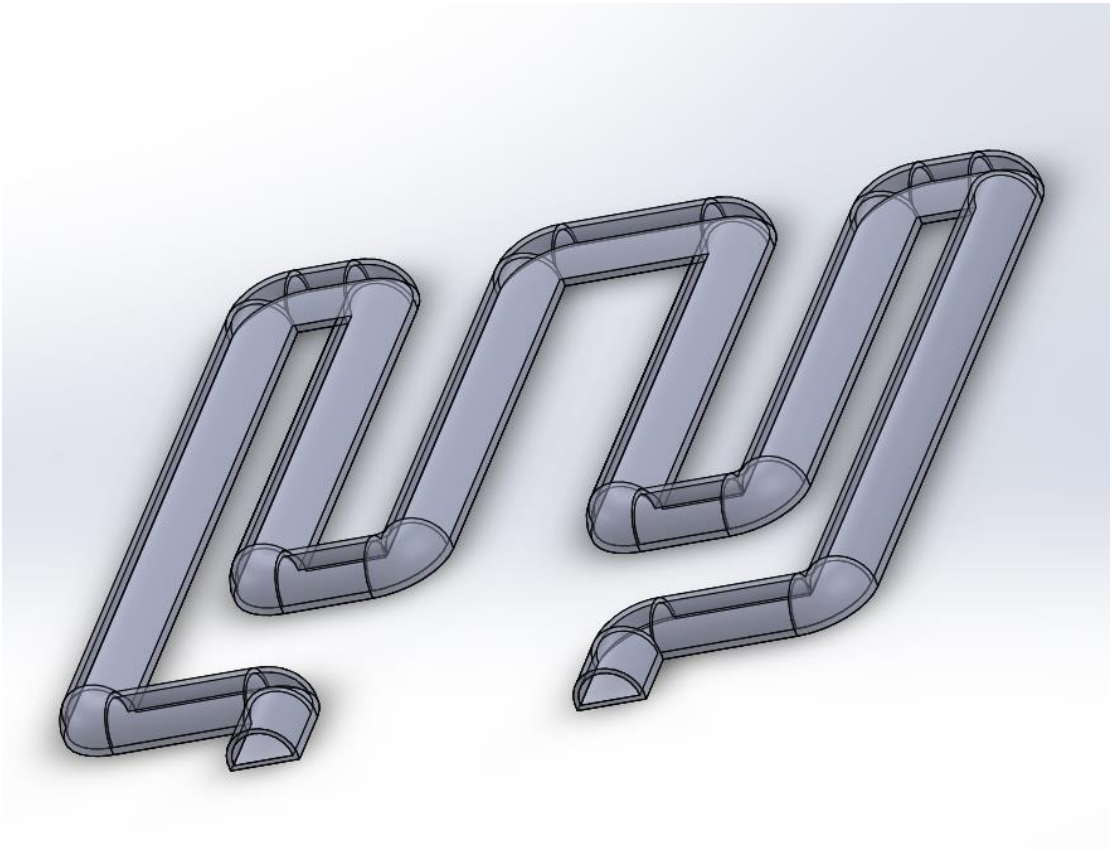

Figure 3. 22 3D model of the cooling pipe

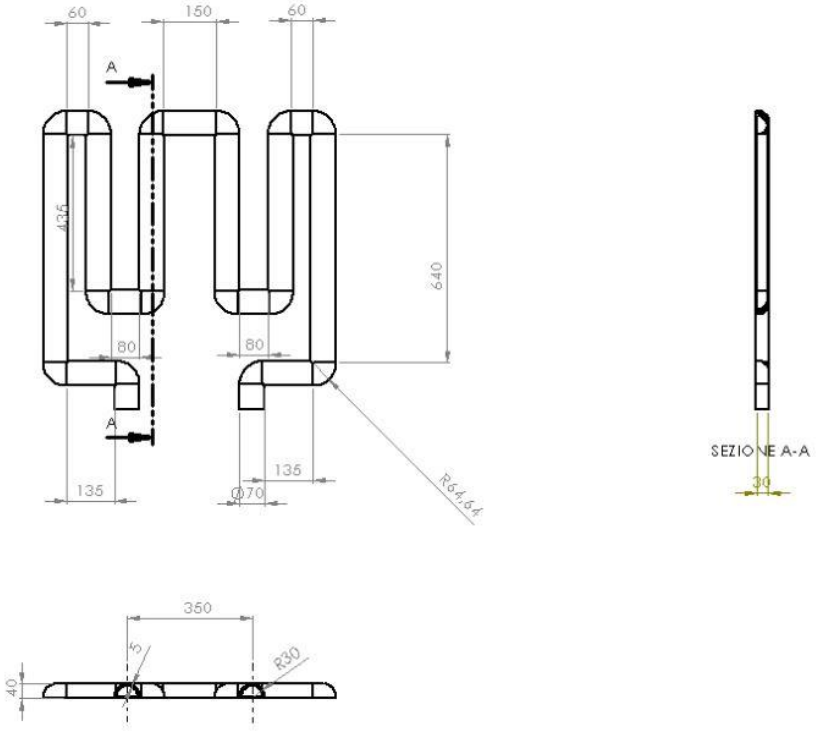

Figure 3. 23 Dimension of the cooling pipe

Here we ensure the minimum heat transfer area, and let it distribute as wide as possible.

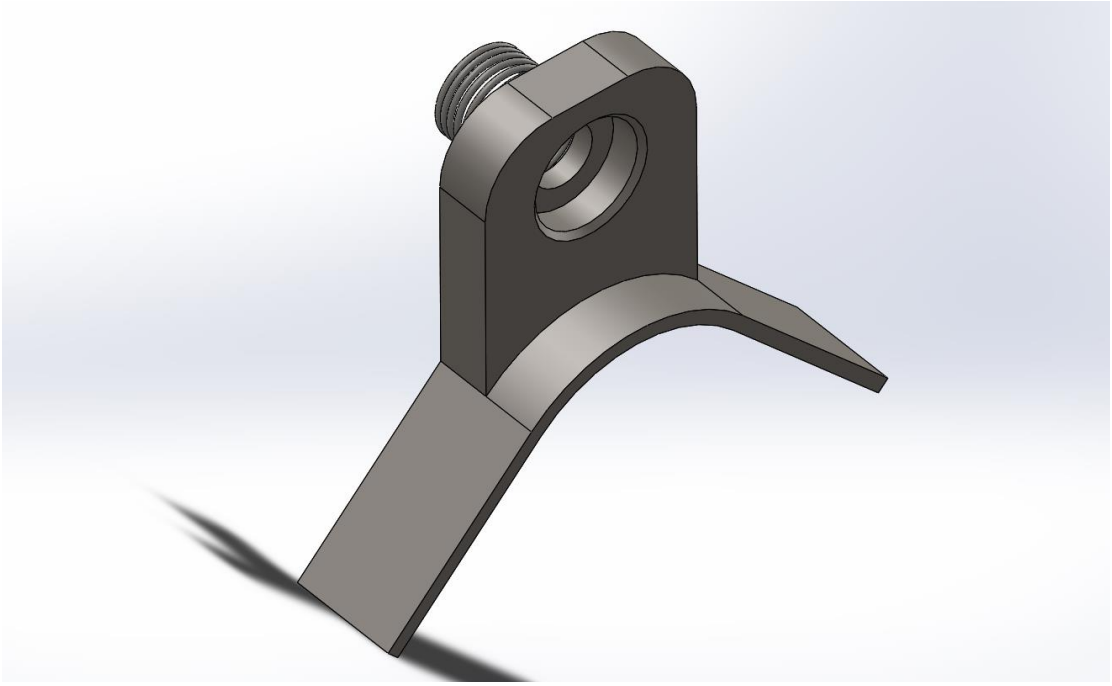

Figure 3. 24 3D model of the bracket for fixture

In order to test the extreme working condition, the initial temperature of the WPT is 65° C .We set the simulation time to 5 minutes to verify whether the temperature of WPT can be cooled down from 65°C. The results are shown following:

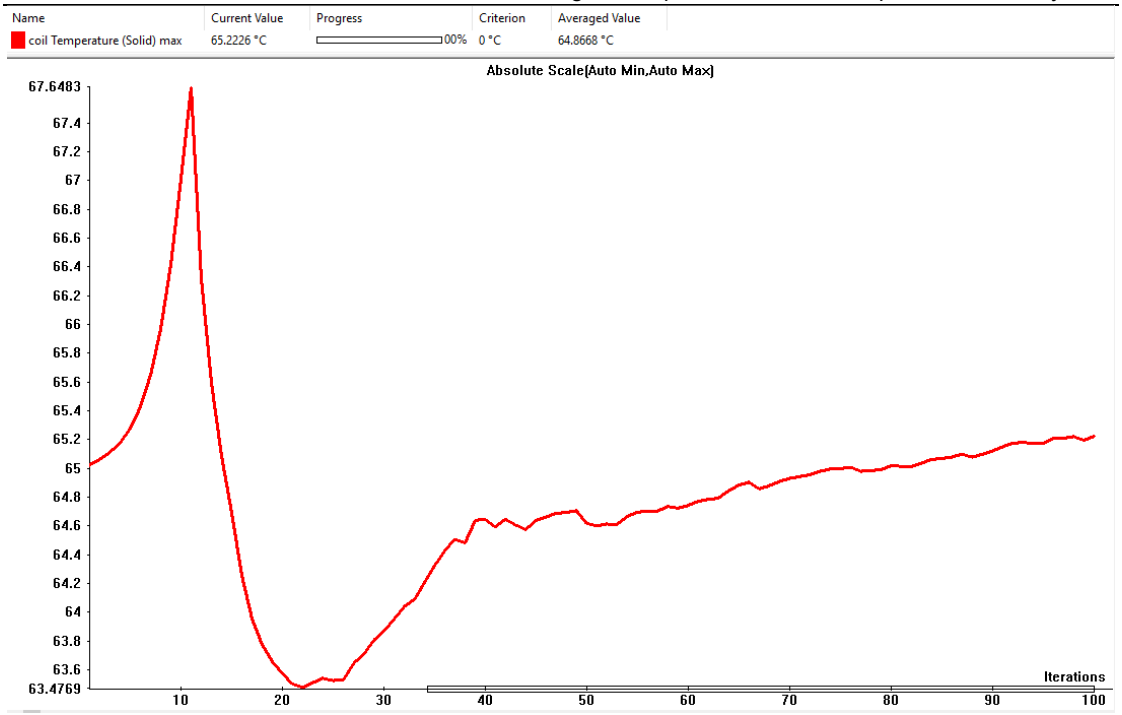

Figure 3. 25 Maximum temperature of the coil

As the figure illustrating, the average temperature can be reduced effectively, although it slightly increased when it reaches the minimum value.

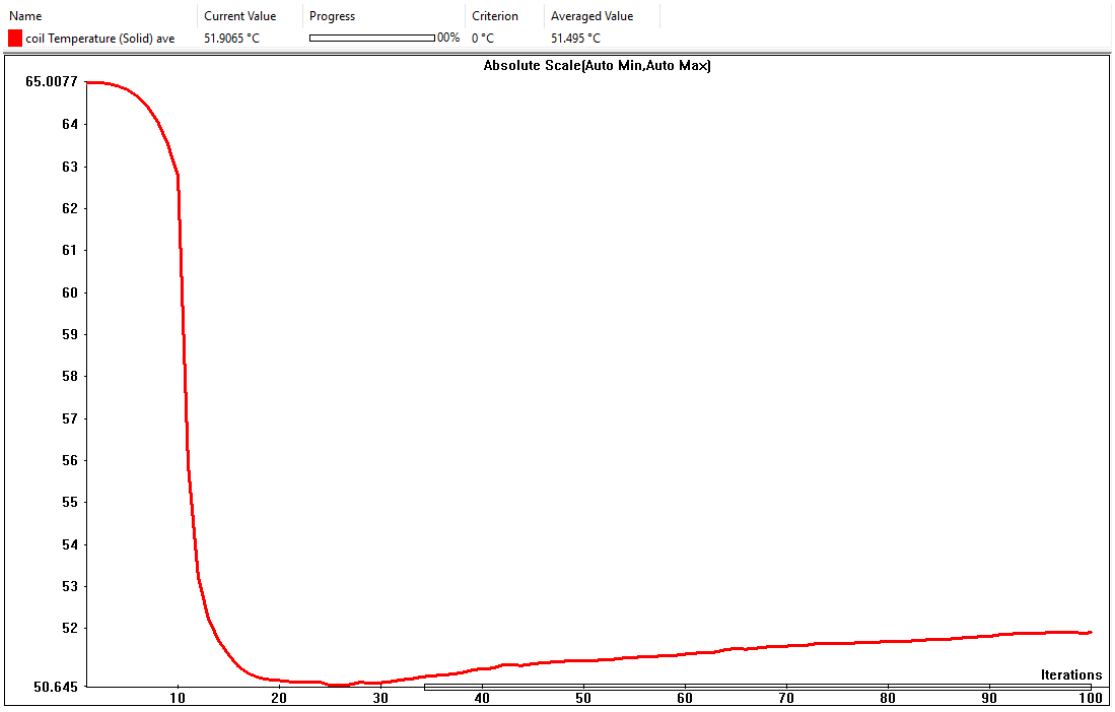

Figure 3. 26 Average temperature of the coil

We find that there is a peak value which exceed our requirement by approximately 2.565°

C at the beginning of the cooling process. Thus, the result can't be accepted and we must analysis the reason.

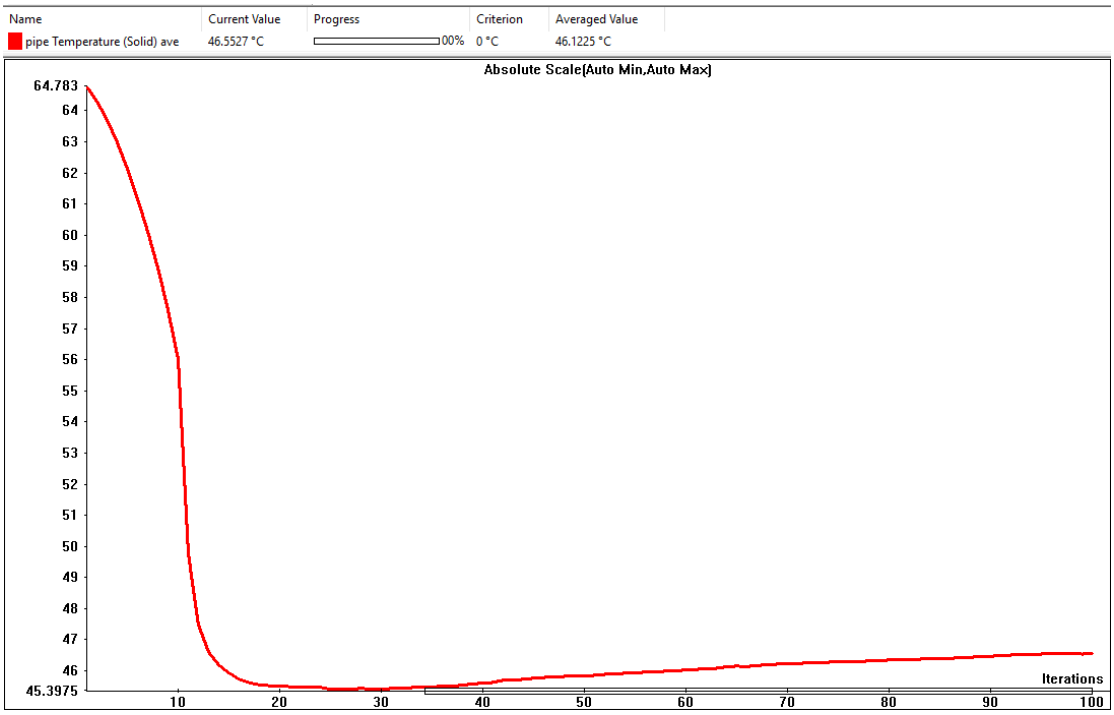

Figure 3. 27 Average temperature of the pipe

The average temperature of pipe is coincident with that of the coil, since they are contacted with each other and heat conduction happens here.

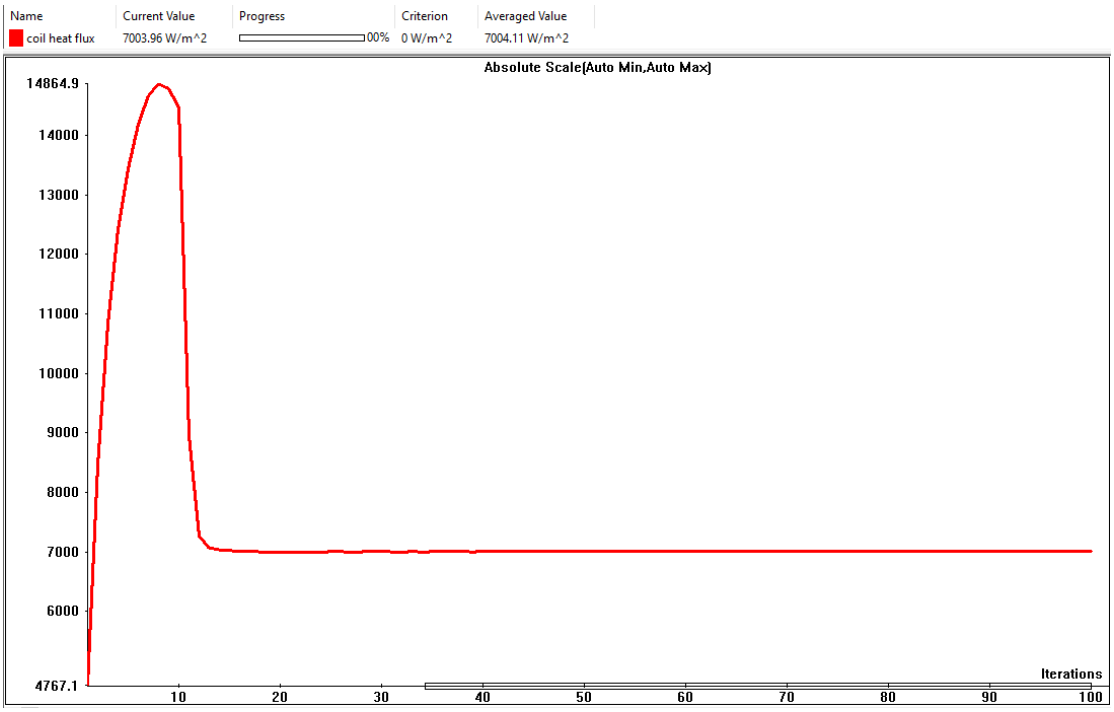

Figure 3. 28 Heat flux of the conduction

Due to the high temperature of WPT set in the beginning, the heat flux reaches its peak value rapidly. Then with the decline of the temperature, the heat flux reduced.

We also make several surface plots below to show a more detailed situation.

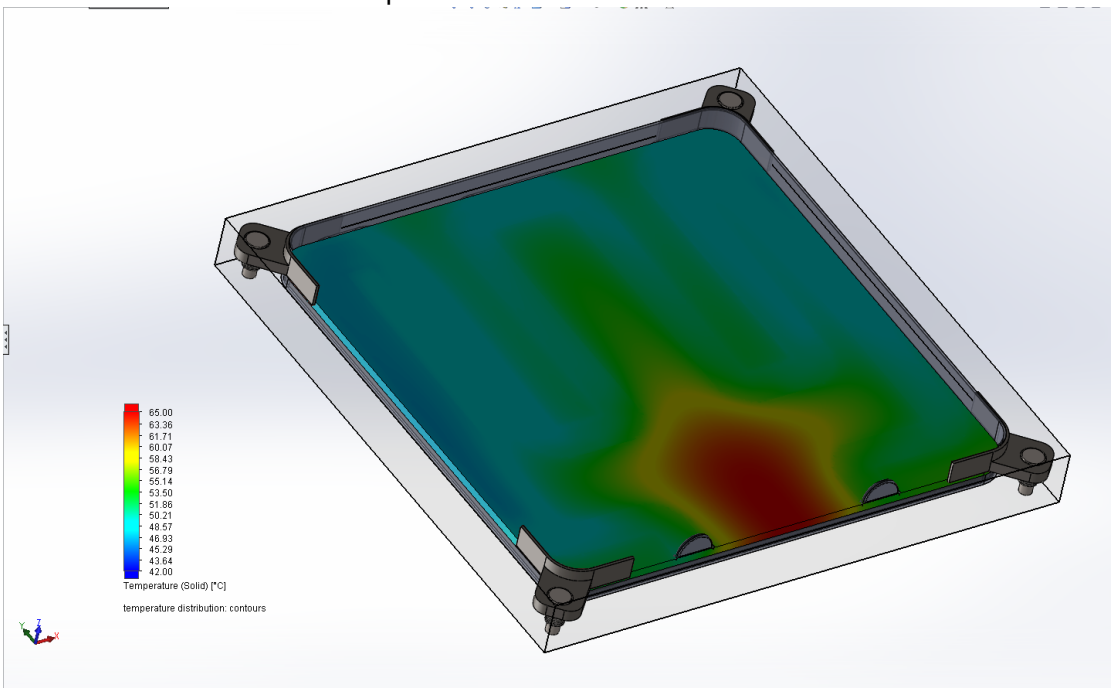

Figure 3. 29 Surface temperature of the coil

There is a large high temperature area distributed on the surface of the coil, which is higher than 65°C, while other area can be cooled down by 10°C.

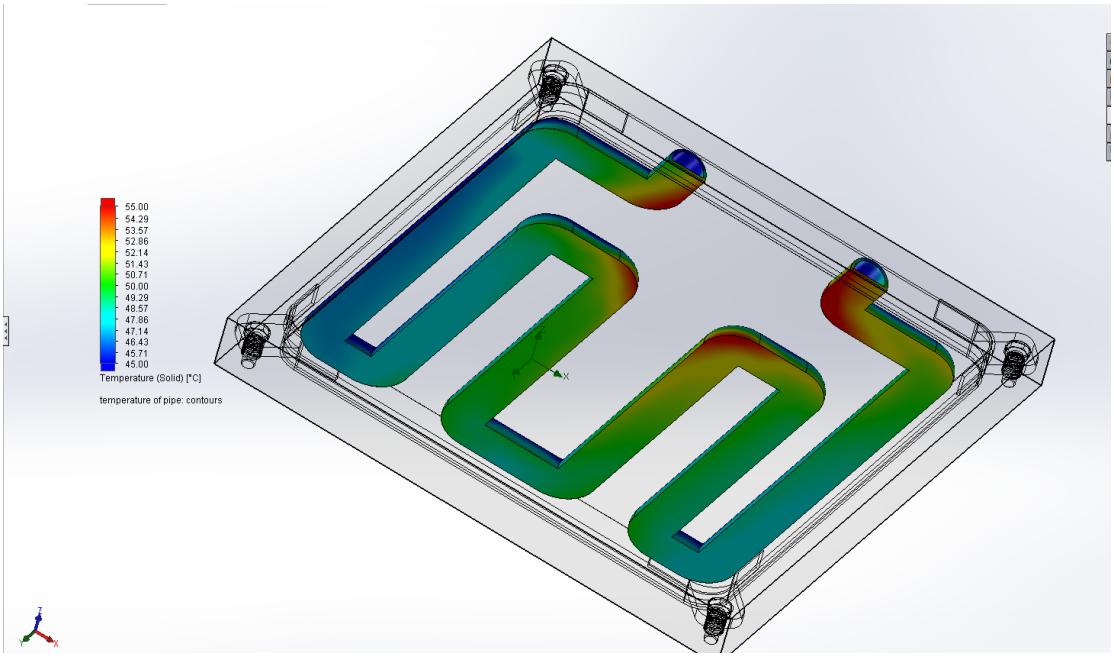

Figure 3. 30 Surface temperature of the pipe

The same pattern can be found on the surface temperature of the pipe, which is also higher at the same area.

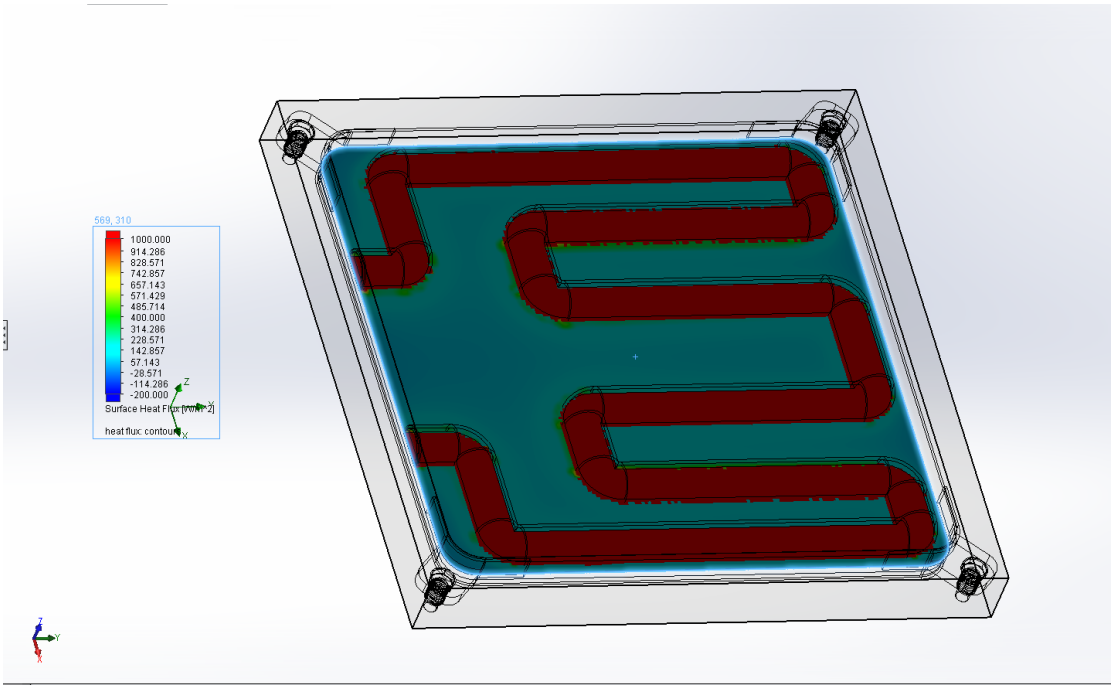

Figure 3. 31 Heat flux of the pipe

The distribution of heat flux is substantially even on the pipe.

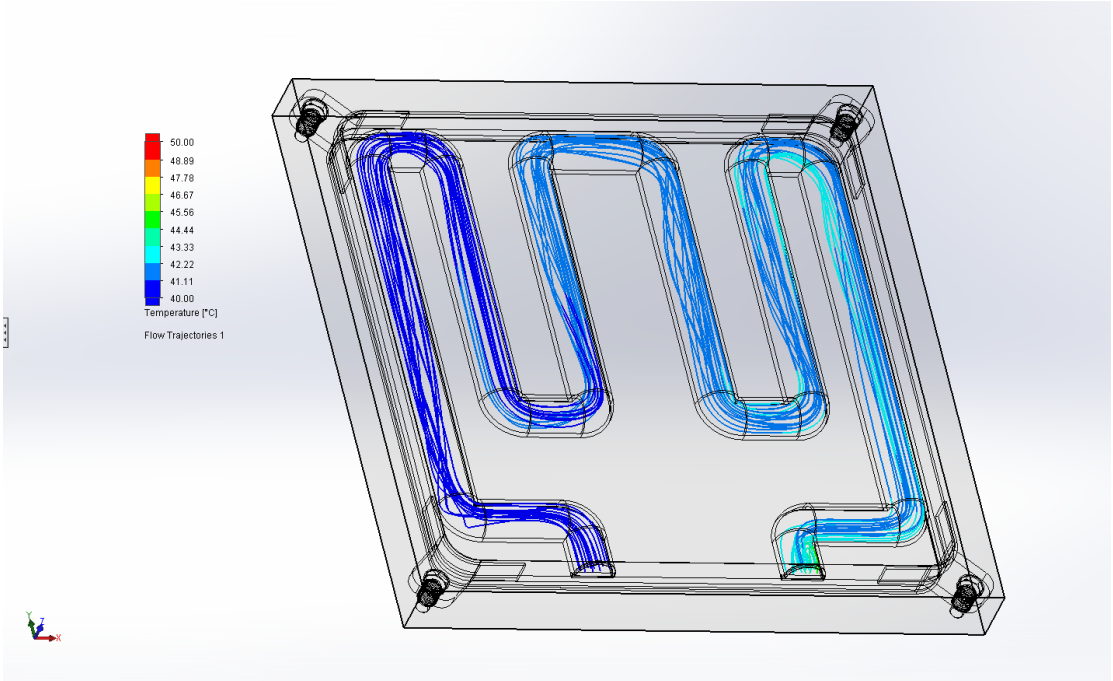

Figure 3. 32 The temperature distribution of the coolant

The coolant is heated from inlet to the outlet through forced heat convection and its

temperature gratitude is about 5°C, consistent with our assumption.

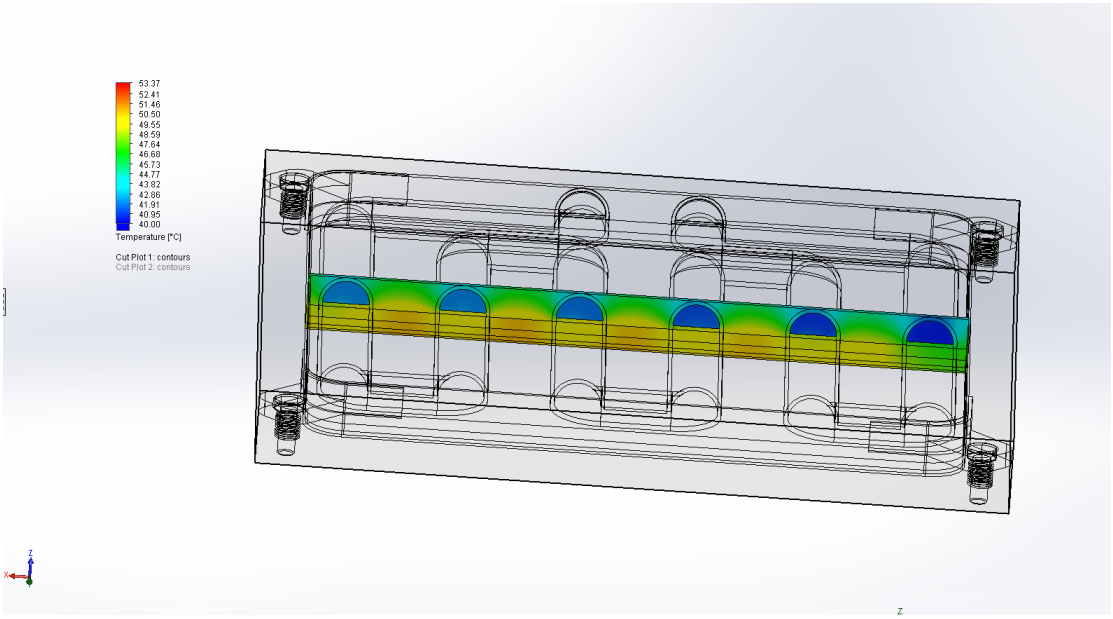

Figure 3. 33 The temperature on the section surface (1)

The position in which the pipe is located has an acceptable temperature, lower than 55°C.

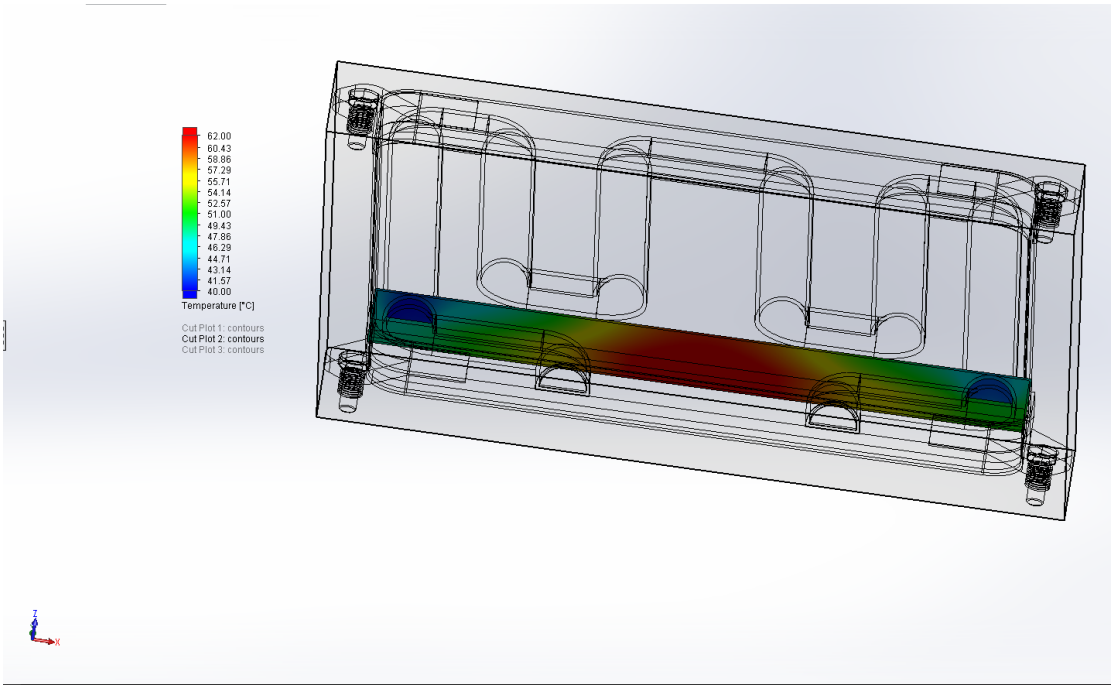

Figure 3. 34 The temperature on the section surface (2)

The position in which the pipe is not located has an unacceptable temperature, higher than 65°C.

Therefore, the simulation result is not completely coincident with our theoretic design

because the average temperature is acceptable while the maximum temperature outstrips our criteria. We must modify our model.

3.2.3 Analysis of the simulation result of the cooling system

From our first simulation result, we found that the high temperature area occurs near the inlet and outlet part of the pipe. The distance between the inlet and outlet is excessively large so that the heat generated at this position cannot be transferred immediately. Instead, it accumulates in the coil at this area, leading to the high temperature. Thus, although the average temperature is acceptable, proved by our analysis before, the maximum temperature is still over the requirement. In the second trial, we modify this distance to check our analysis.

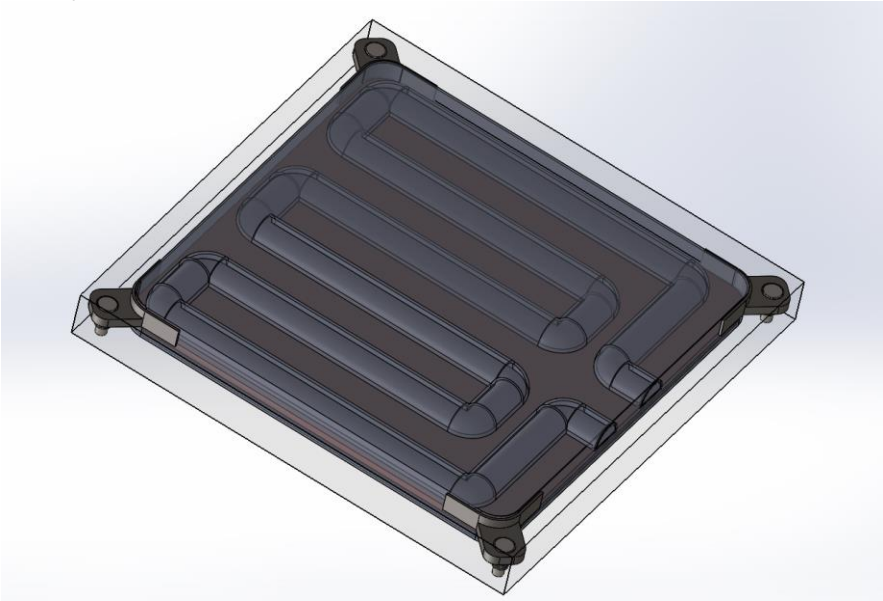

Figure 3. 35 3D model of the cooling system after modification

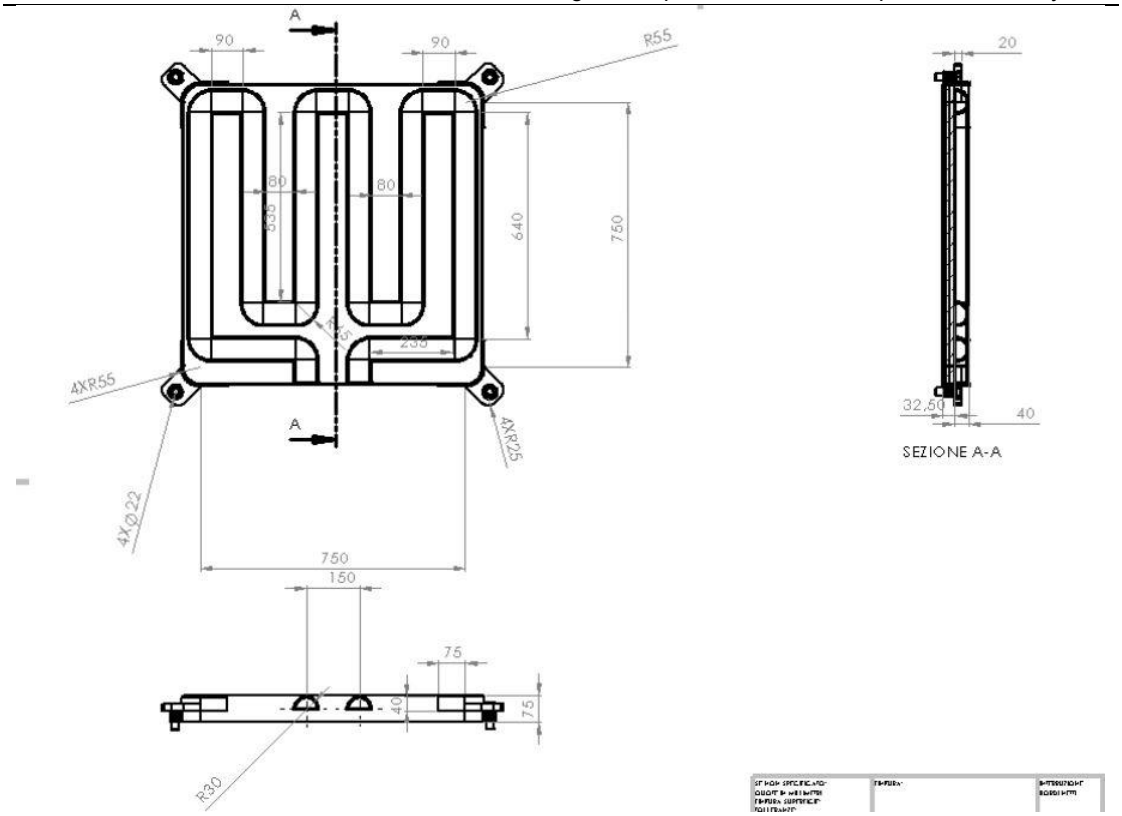

Figure 3. 36 Dimension of the cooling system after modification

Here we also ensure the minimum heat transfer area as before, and the distance between the coolant inlet and outlet has been reduced.

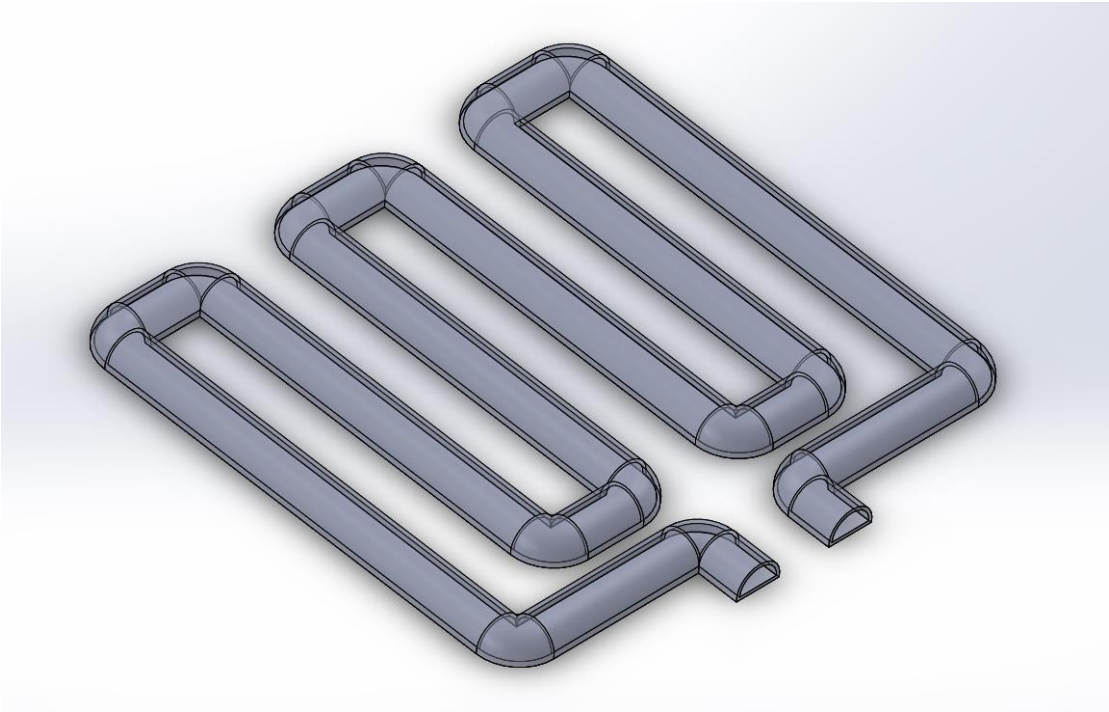

Figure 3. 37 3D model of the cooling pipe after modification

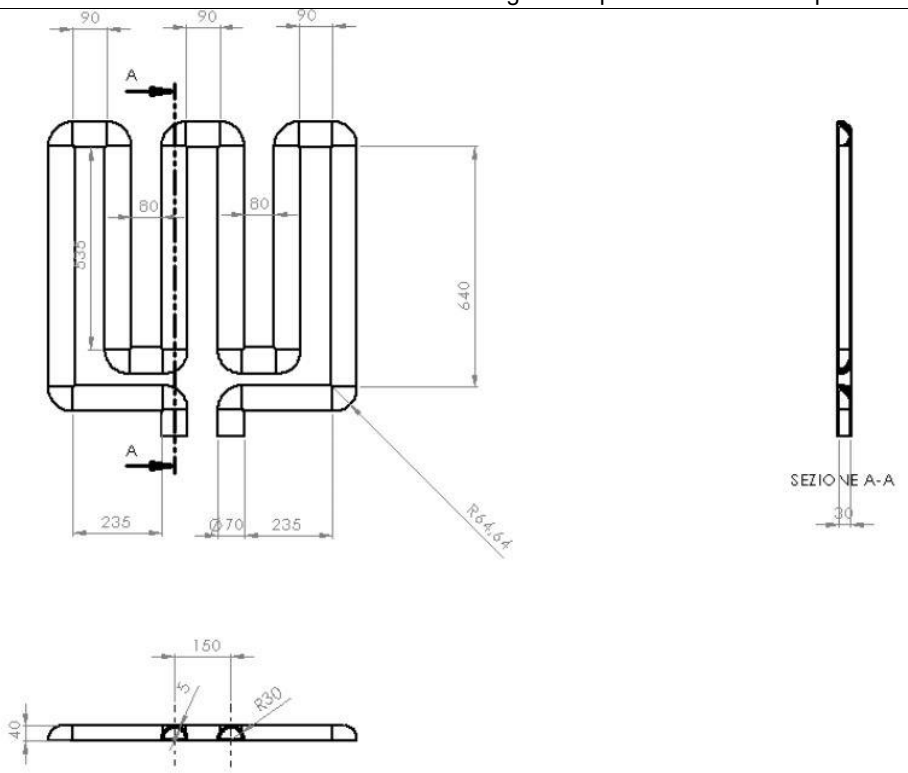

Figure 3. 38 Dimension of the cooling pipe after modification

In order to test the extreme working condition, the initial temperature of the WPT is still 65° C .We set the simulation time to 5 minutes as before to verify whether the temperature of WPT can be cooled down from 65°C, especially the maximum temperature. The results are shown following:

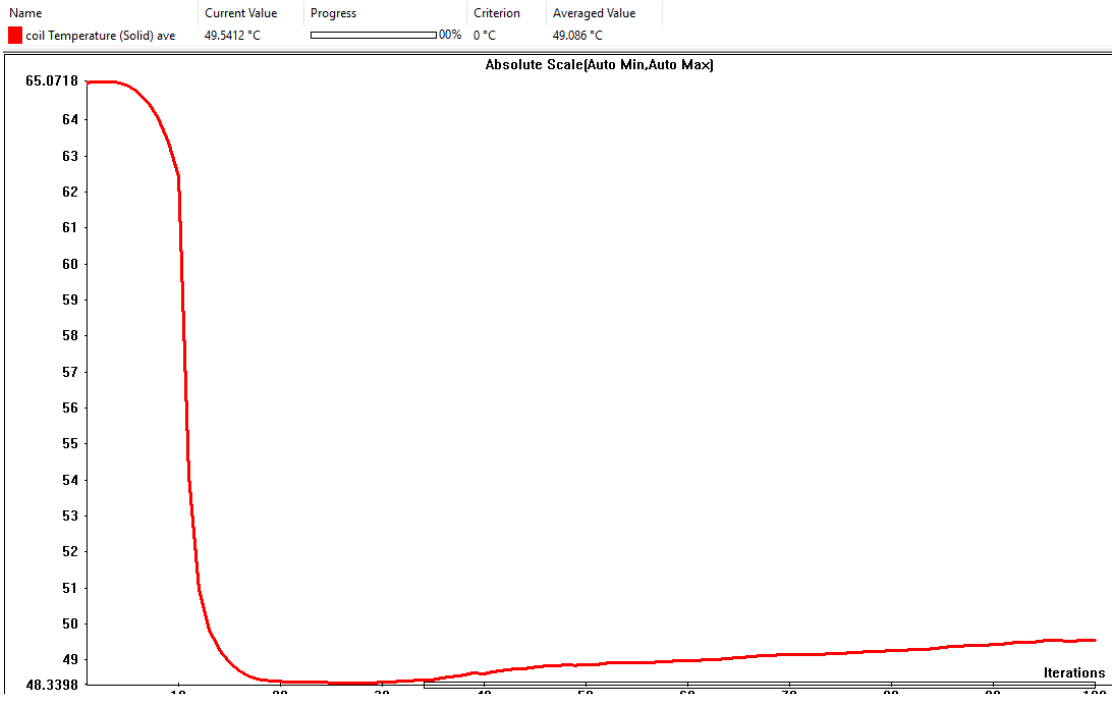

Figure 3. 39 Average temperature of the coil after modification

As the figure illustrating, the average temperature still can be reduced effectively, although it slightly increased when it reaches the minimum value. The absolute value also reduced compared with the situation in the first trial.

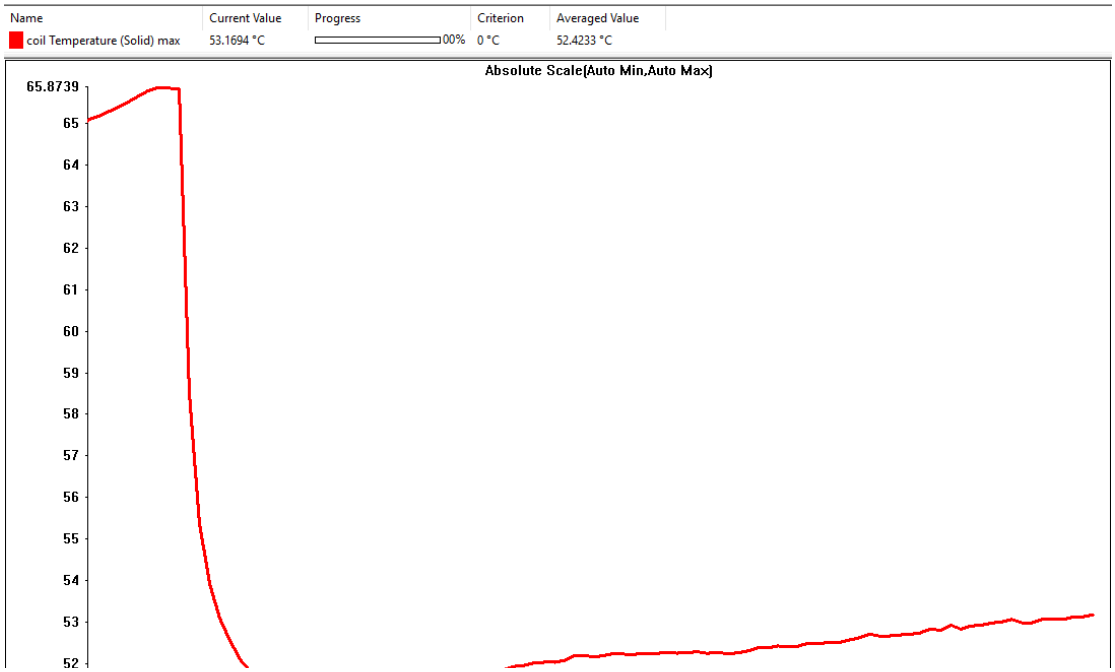

Figure 3. 40 Maximum temperature of the coil after modification

We find that there is also a peak value which is about 0.9°C higher than our requirement at the beginning of the cooling process. Because we have already set the coil temperature at 65°C. Thus, we regard the result as acceptable.

Figure 3. 41 Average temperature of the pipe after modification

The average temperature of pipe is still coincident with that of the coil and the absolute value also reduced compared with the situation in the first trial.

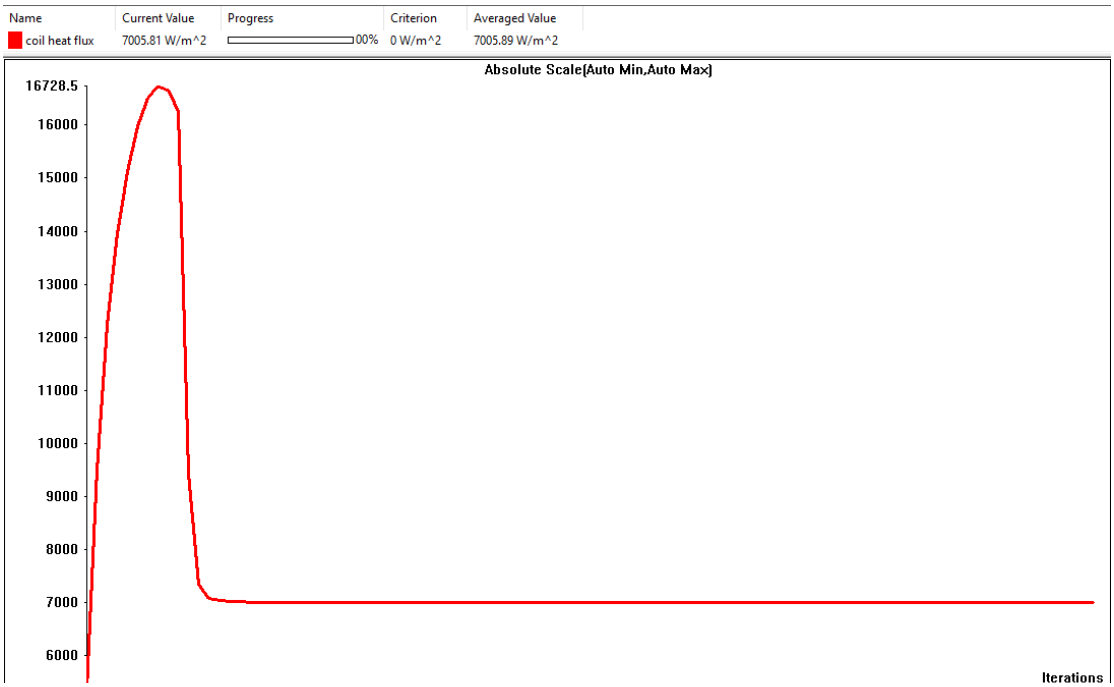

Figure 3. 42 Heat flux of the conduction after modification

Due to the coolant receive more heat from the high temperature area where heat is accumulated in the first trial, we can find both the peak value increased slightly,

We now verify the surface temperature of the coil.

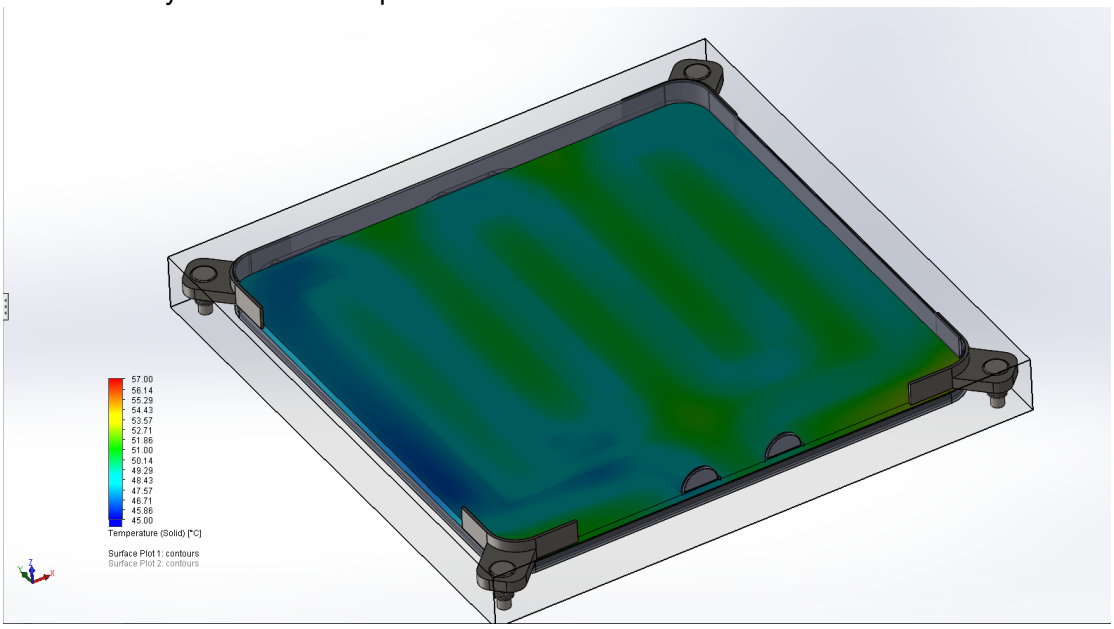

Figure 3. 43 Surface temperature of the coil after modification

The high temperature area on the surface of the coil disappeared, all of the area is lower than 65°C, which is cooled down by 10°C.

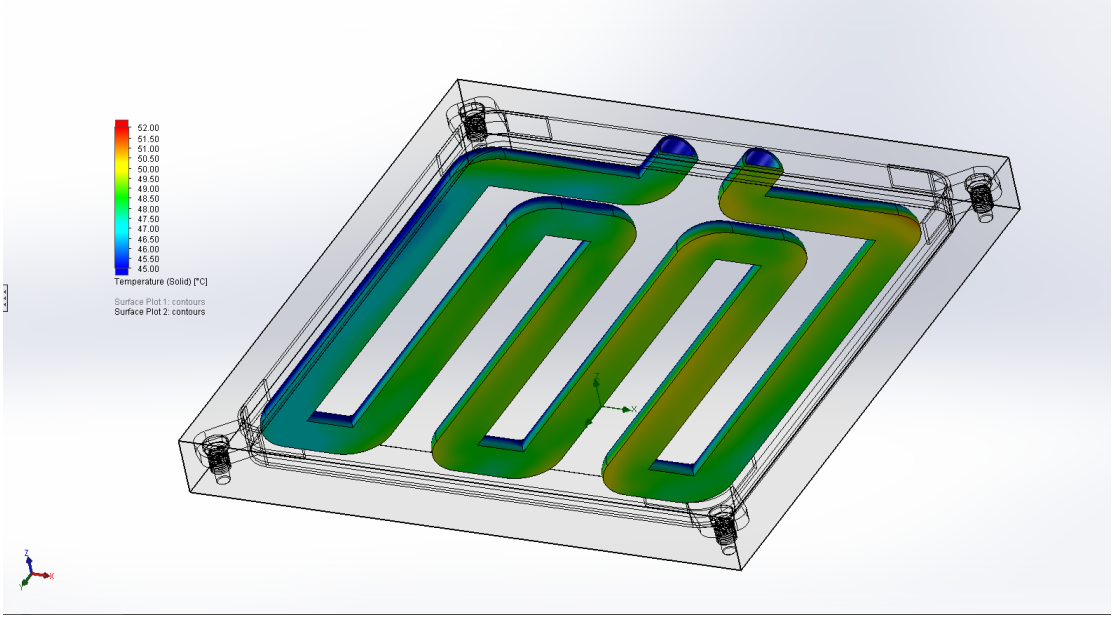

Figure 3. 44 Surface temperature of the pipe after modification

The same pattern can be found on the surface temperature of the pipe, the high temperature area also disappeared.

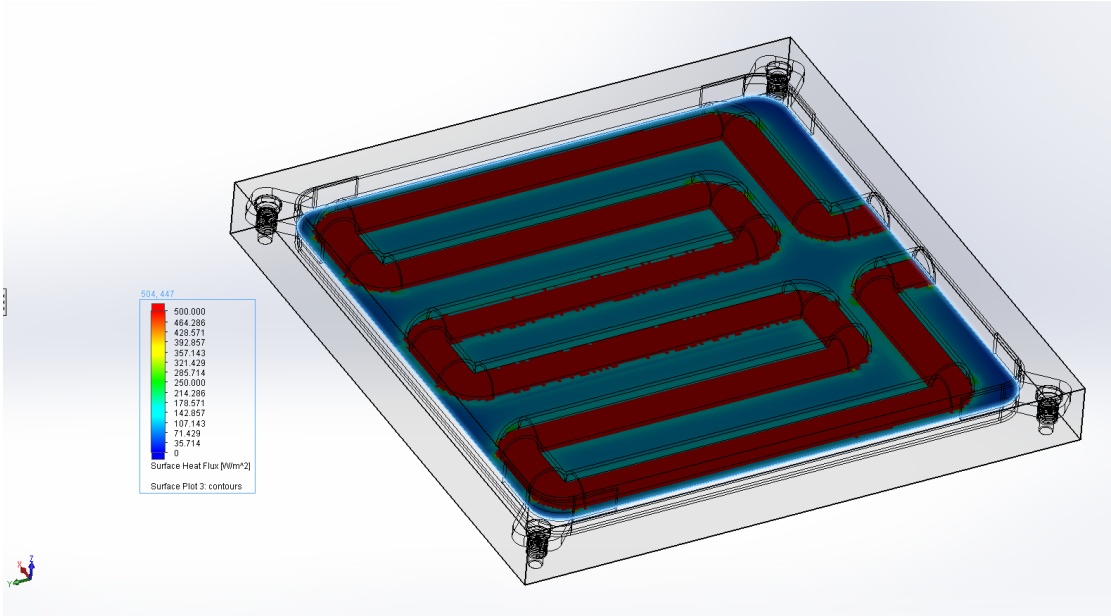

Figure 3. 45 Heat flux of the pipe after modification

The distribution of heat flux is still substantially even on the pipe.

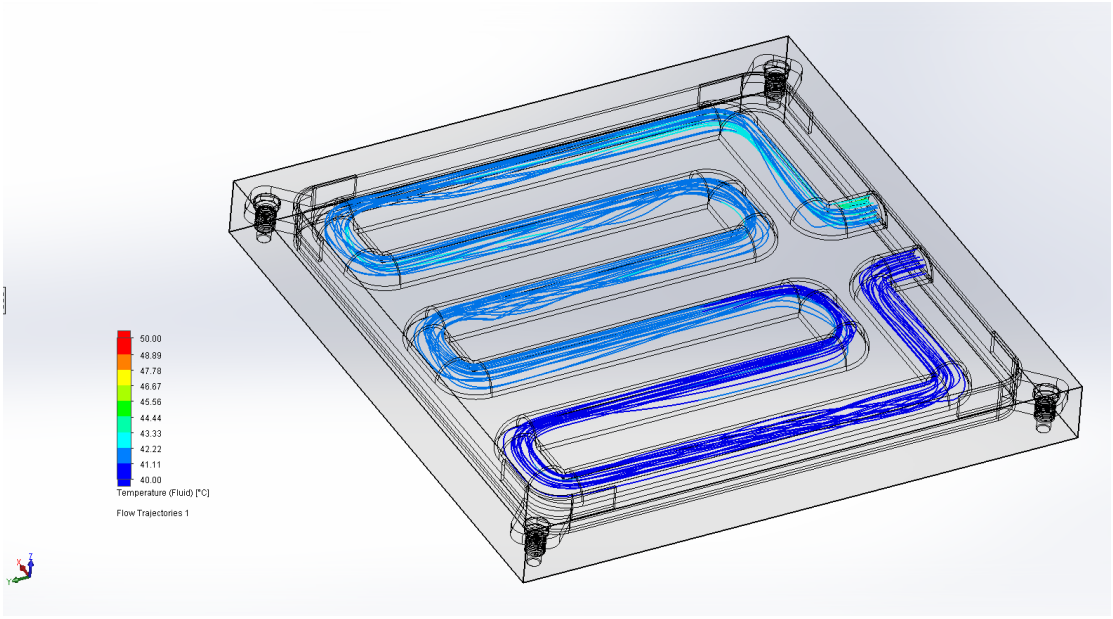

Figure 3. 46 The temperature distribution of the coolant after modification

The coolant is heated from inlet to the outlet through forced heat convection and its temperature gratitude is about 5°C, the same as before.

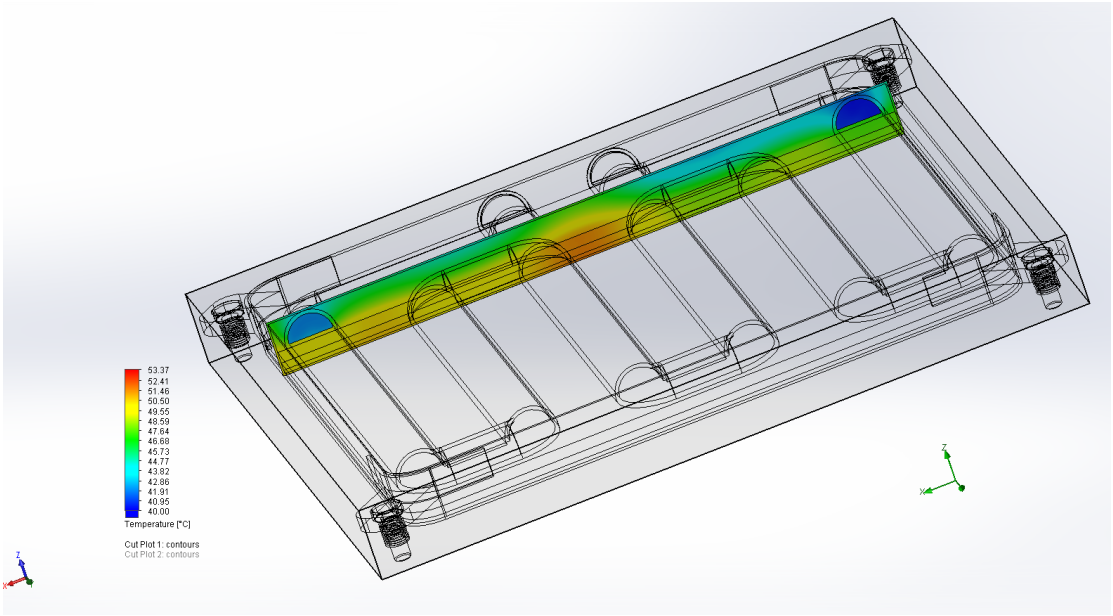

Figure 3. 47 The temperature on the section surface after modification

All of the surface of the coil has an acceptable temperature, lower than 55°C. Thus, after guaranteeing every point is not far from the coolant pipe, the heat is not accumulated anymore so that the temperature is reduced successfully. This configuration can verify our design.

4. Analysis and design of the vibration oriented mechanism of the wireless power transfer system on electric vehicle

4.1 Analysis of the vibration oriented mechanism

Since the WPT system will be imposed load during the vibration generated from the road, we decide to choose four threaded fasteners located at the four corners to ensure the reliability of the fixture.

First, it is necessary to simplify the working condition of these threaded fasteners: the vibration can be considered as the alternating tensile stress acting on the axial direction of the bolts. Thus, we introduce the theories of alternate stress.

4.1.1 Theories of the stress variation on components and calculation of the strength of components

There are three cases about the law of stress variation on parts.

1. The stress ratio r is a constant

$$r = \frac{\sigma_{min}}{\sigma_{max}}$$

Under the premise of a simple loading condition, **r = C**. Where r is the stress ratio and C is a constant. In this situation the strength calculation is to compute the maximum stress safety factor. The strength condition is:

$$n_\sigma = \frac{\sigma'_{max}}{\sigma_{max}} = \frac{\sigma_{-1}}{K_\sigma \cdot \sigma_a + \Psi_\sigma \cdot \sigma_m} \geq [n] \qquad (1)$$

Where:
n_σ = maximum stress safety factor of components

σ'_{max} = maximum stress of components (N/mm^2)
σ_{max} = maximum received stress of components (N/mm^2)
σ_{-1} = symmetrical cyclic tensile fatigue strength (N/mm^2)
σ_a = alternating stress amplitude of components (N/mm^2)
σ_m = mean stress of components (N/mm^2)
K_σ = comprehensive influence coefficient
ψ_σ = material factor

2. The minimum stress is a constant

In theory, when the minimum value of alternate stress is a constant, that is: $\boldsymbol{\sigma_{min} = C}$. According to the maximum stress, the maximum stress safety factor can be calculated. The strength condition is:

$$n_a = \frac{\sigma'_{max}}{\sigma_{max}} = \frac{2\sigma_{-1} + (K_\sigma - \Psi_\sigma) \cdot \sigma_{min}}{(K_\sigma + \Psi_\sigma) \cdot (2\sigma_a + \sigma_{min})} \geq [n] \qquad (2)$$

3. The mean stress is a constant

In theory, the maximum and minimum value of working alternate stress are constant, that is: $\boldsymbol{\sigma_m = C}$. The strength condition is:

$$n_\sigma = \frac{\sigma'_{max}}{\sigma_{max}} = \frac{\sigma_{-1} + (K_\sigma - \Psi_\sigma) \cdot \sigma_m}{K_\sigma \cdot (\sigma_m + \sigma_a)} \geq [n] \qquad (3)$$

Following these theories of alternate stress in the three cases, the maximum stress safety factor n_σ can be computed, which should be no less than the allowable stress safety factor [n] in order to guarantee the safety during working. However, the above situations may not actually occur in isolation. Therefore, the choice of the formula for the calculation should be based on the law of the possible changes in the stress of the specific component.

4.1.2 Calculation method of fatigue strength of bolts subjected to unidirectional constant alternating load

1. Force analysis of the bolts

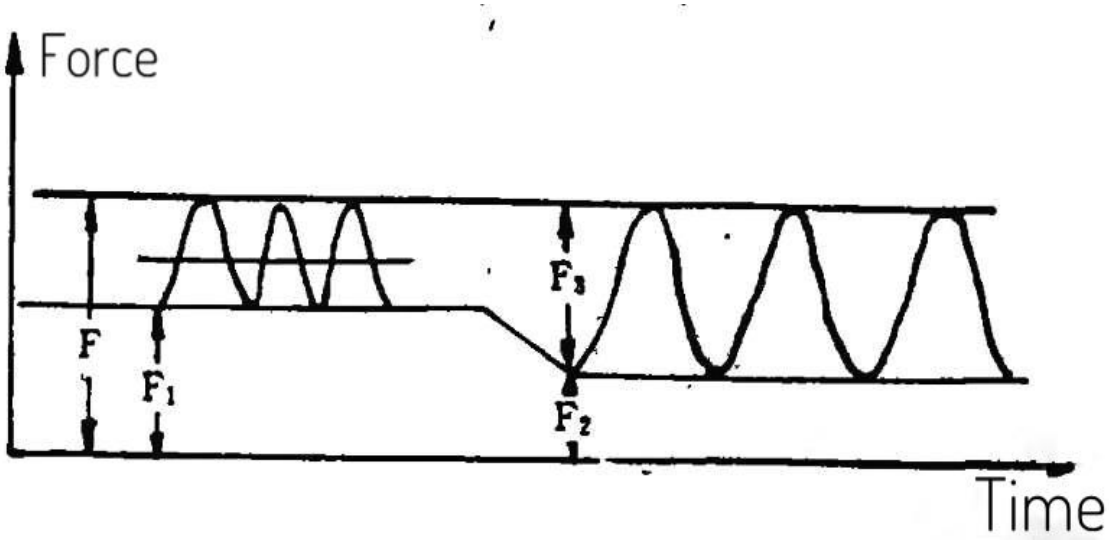

Figure 4. 1 Alternate stress

As can be seen from Figure, the bolt as a fastening part to withstand the constant alternating load, after the role of the pre-tightening force F_1 (without considering the friction torque case), withstand the tension between 0 ~ F_3, bolts received by the total tension varying between F_1 and F. When the bolt is subjected to a cyclical fluctuating working load from 0 to F_3, its internal stress is an asymmetric cyclic variable stress, and the total tensile load it receives is periodically fluctuating between the remaining preloads F_2 and F_3. At this time, the bolt is subjected to unidirectional stable stress.

2. Calculated theoretical basis and calculation method

According to the basic theory of variable stress loading on parts, we can better understand the situation of bolts subjected to variable stress and the calculation of fatigue strength. Some mature viewpoints have been formed, that is, under the premise of the law of variable stress, the maximum stress safety factor can be used to check the strength. Several major ideas and calculation methods are described below.

2-a. Minimum variable stress maintains unchanged

$$\sigma_{min} = \frac{F_1}{\frac{\pi d^2}{4}}$$

Where:

F_1 = pre-tightening force

d = nominal diameter of the bolt, a constant

So σ_{min} = C. The equation (2) can be used for the calculation of fatigue strength of the bolts, that is:

$$n_a = \frac{2\sigma_{-1} \cdot (K_\sigma - \Psi_\sigma) \cdot \sigma_{min}}{(K_\sigma + \Psi_\sigma) \cdot (2\sigma_a + \sigma_{min})} \geq [n]$$

When this condition is met, the safety can be guaranteed.

2-b. The main influencing factor of fatigue strength is cyclic alternating stress amplitude

$$n_\sigma = \frac{[\sigma_a]}{\sigma_a} \geq [n_a]$$

Where:

$$[\sigma_a] = \frac{\sigma_{-1}}{[n_a] \cdot k_\sigma}$$

k_σ is the effective stress concentration factor. When this condition is met, the safety can be guaranteed.

2-c. Simplification from asymmetrical cycle to symmetrical cycle

In this method, r = C. The equation (1) can be used for the calculation of maximum stress safety factor, that is:

$$n_\sigma = \frac{\sigma_{-1}}{K_\sigma \cdot \sigma_a + \Psi_\sigma \cdot \sigma_m} \geq [n]$$

When this condition is met, the safety can be guaranteed.

4.2 Optimized design of the vibration oriented mechanism

In our case, the bolts on the WPT system will be subjected to variable stresses during the travel of vehicle. Due to the limited information given, there are several important assumptions placed to complete the designing phase. According to the previous calculation, the weight of coil is 46.0955 kg. Considering it is placed into a box with other electric elements, we assume the total weight of the system is 100 kg. Thus, the four bolts will be imposed a 981N force, each 245.25N as static load. However, due to the unevenness of road, the tire pressure and the characteristic of vehicle's suspension system,

the bolts will be subjected to a variable load. An assumption is made that the maximum force F_t applied on each bolt is 300% of the WPT system's weight, and the working load varies from 100% to 300% weight, which can fully represent the extreme working condition. Thus, the four bolts get a 981~2943N working force (F_t). Besides, we assume that the residual pre-tightening force (F_2) equals to 1.5 times working load. We choose 1035 steels (carbon steel, American standards), property class 5.6, as the bolts material.

1. Calculation of the maximum working load on each bolt

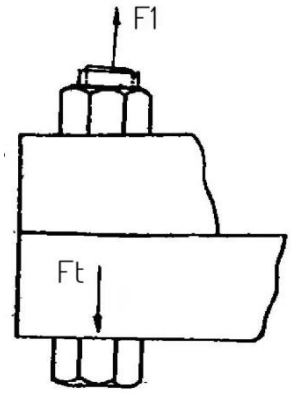

Figure 4. 2 Working force (Ft) on bolts

$$q = \frac{F_t}{4} = 735.75\ N$$

Thus, the maximum working load for each bolt is 735.75N. And the working load of varies between 245.25~735.75N.

2. Calculation of the residual pre-tightening force on each bolt

$$F_2 = 1.5q = 1103.625\ N$$

Thus, the residual pre-tightening force for each bolt is 1103.625N.

3. Calculation of the maximum tension force on each bolt

$$F = q + F_2 = 1839.375\ N$$

Thus, the maximum tension force for each bolt is 1839.375N.

4. Calculation of the pre-tightening force on each bolt

$$F_1 = F - \frac{C_1}{C_1 + C_2} \cdot q = F - K_c \cdot q = 1250.775\ \mathrm{N}$$

Where the K_c is the relative stiffness of bolts, in relation to the materials of the gasket.

Material	Metal（or no gasket）	Leather	Copper-asbestos	Rubber
K_c	0.2~0.3	0.7	0.8	0.9

Table 4. 1 Relative stiffness of bolts

Here we assume copper asbestos gasket, so K_c =0.8.
Thus, the pre-tightening force for each bolt is 1250.775N

5. Calculation of the allowable stress

No.	Mechanical or physical property		Property class									
			4.6	4.8	5.6	5.8	6.8	8.8		9.8	10.9	12.9/12.9
								d≤16mm [a]	d>16mm [b]	d≤16mm		
1	Tensile strength, *R*m, MPa	nom. [c]	400		500		600	800		900	1000	1200
		min.	400	420	500	520	600	800	830	900	1040	1220
2	Lower yield strength, *R*eL d, MPa	nom. [c]	240	-	300	-	-	-	-	-	-	-
		min.	240	-	300	-	-	-	-	-	-	-
3	Stress at 0,2 % non-proportional elongation,	nom. [c]	-	-	-	-	-	640	640	720	900	1080
		min.	-	-	-	-	-	640	660	720	940	1100

	$R_{p0,2}$, MPa											
4	Stress at 0,0048 *d* non-proportional elongation for full-size fasteners, R_{pf}, MPa	nom. [c]	-	320	-	400	480	-	-	-	-	-
		min.	-	340 [e]	-	420 [e]	480 [e]	-	-	-	-	-
5	Stress under proof load, S_p [f], MPa	nom.	225	310	280	380	440	580	600	650	830	970
	Proof strength ratio $S_{p,nom}/R_{eL\ min}$ or $S_{p,nom}/R_{p0,2\ min}$ or $S_{p,nom}/R_{pf\ min}$		0.94	0.91	0.93	0.90	0.92	0.91	0.91	0.90	0.88	0.88
6	Percentage elongation after fracture for machined test pieces, *A*, %	min.	22	-	20	-	-	12	12	10	9	8
7	Percentage reduction of area after fracture for machined	min.	-					52		48	44	44

	test pieces, *Z*, %											
8	Elongation after fracture for full-size fasteners, A_f	min.	-	0.24	-	0.22	0.20	-	-	-	-	-
9	Head soundness		No fracture									
10	Vickers hardness, HV *F* ≥98 N	min.	120	130	155	160	190	250	255	290	320	385
		max.	220 [g]				250	320	335	360	380	435
11	Brinell hardness, HBW $F = 30\ D^2$	min.	114	124	147	152	181	238	242	276	304	356
		max.	209 [g]				238	304	318	342	361	414
12	RockWell hardness, HRB	min.	67	71	79	82	89	-				
		max.	95.0 [g]				99.5	-				
	RockWell hardness, HRC	min.	-					22	23	28	32	39
		max.	-					32	34	37	39	44

13	Surface hardness, HV 0,3	max.	-			h			h, i	h, j
14	Height of non-decarburized thread zone, *E*, mm	min.	-			1/2 H_1			2/3 H_1	3/4 H_1
	Depth of complete decarburization in the thread, *G*, mm	max.	-			0.015				
15	Reduction of hardness after re-tempering, HV	max.	-			20				
16	Breaking torque, M_B, N·m	min.	-			in accordance with ISO 898-7				
17	Impact strength, K_V [k, l], J	min.	-	27	-	27	27	27	27	m
18	Surface integrity in accordance with		ISO 6157-1 [n]							ISO 6157-3

a. A value does not apply to structural bolting.
b. Structural bolt connection d≥M12.
c. The nominal value is only for the designated system of the property category.
d. Allow to measure the stress at 0.2% non-proportional elongation $R_{p0,2}$ when the lower yield strength R_{eL} cannot be determined.
e. For attribute classes 4.8, 5.8 and 6.8, the value of R_{pf} min is under

investigation. The present value given is only used to calculate the verification stress ratio. They are not test values.
f. Prove the loads specified.
g. The hardness of the end of the fastener should be 250 HV, 238 HB or 99.5 HRB.
h. When the hardness of the surface and the hardness of the core are measured with HV 0,3, the surface hardness shall not exceed the 30-dimensional Vickers point of the hardness measured on the fastener.
i. Any increase in surface hardness indicates that surface hardness exceeding 390 HV is unacceptable.
j. Any increase in surface hardness indicates that surface hardness exceeding 435 HV is unacceptable.
k. The value is determined at a test temperature of 20°C.
l. Suitable for d≥16mm.
m. The value of m KV is under investigation.
n. In place of ISO 6157-1, ISO 6157-3 can be applied by agreement between the manufacturer and the purchaser.

Table 4. 2 Mechanical and physical properties of bolts, screws and studs[43]

Load properties	Allowable stress	Safety factor without control of pre-tightening force [n]				Safety factor with control of pre-tightening force [n]
Static load	$[\sigma]=\frac{R_{eL}}{[n]}$	Material	Diameter			Regardless of diameter
			M6~M16	M16~M30	M30~M60	
		Carbon steel	4~3	3~2	2~1.3	1.2~1.5
		Alloy steel	5~4	4~2.5	2.5	
Dynamic load	According to maximum stress $[\sigma_t]=\frac{R_{eL}}{[n]}$	Carbon steel	10~6.5	6.5	6.5~10	1.2~1.5
		Alloy steel	7.5~5	5	5~7.5	
	According to cyclic	$[n_a]=2.5\sim5$				$[n_a]=1.5\sim2.5$

	alternating stress amplitude $[\sigma_a] = \frac{\varepsilon \cdot \sigma_{-1p}}{[n_a] \cdot k_\sigma}$		

1. σ_{-1p} is the tensile and compressional fatigue limit of material (see Table 4.4)
2. ε is the dimensional factor (see Table 4.5)
3. k_σ is the effective stress concentration factor (see Table 4.6)

Table 4. 3 Allowable safety factor [n][44]

Material	10	Q235-A	35	45	40Cr
σ_{-1p}	120~150	120~160	170~220	190~250	240~340

Table 4. 4 Tensile and compressional fatigue limit of material

Diameter/mm	<12	16	20	24	30	36	42	48	56	64
ε	1	0.87	0.8	0.74	0.65	0.64	0.60	0.57	0.54	0.53

Table 4. 5 Dimensional factor

Tensile strength R_m/MPa	400	600	800	1000
k_σ	3	3.9	4.8	5.2

Table 4. 6 Effective stress concentration factor[45]

From the tables above, we found the parameter needed. Since in our assumption we control the pre-tightening force, and

5-a. The bolts get a static load, we choose the maximum value in the range, [n] = 1.5;

5-b. The bolts get a dynamic load, we choose the maximum value in the range, [n] = 1.5;

5-c. The bolts get a dynamic load with cyclic alternating stress amplitude, we choose the maximum value in the range, $[n_a]$ = 1.5;

In order to decide the dimension of bolts, we use static strength [σ] in case 5-a for calculation. For 1035-steel, property class 5.6, its yield strength R_{eL} = 300 N/mm^2.

$$[\sigma] = \frac{R_{eL}}{[n]} = 200\ N/mm^2$$

So [σ] equals to 200 N/mm^2.

6. Calculation of the nominal diameter of the bolts

$$d_1 \geq \sqrt{\frac{4 \times 1.3 \cdot F}{\pi \cdot [\sigma]}} = 3.902\ mm$$

So, the thread trails d_1 should no less than 3.03 mm.

$$d_1 = d - 1.0825 \cdot P$$

Size - Nominal Diameter *(mm)*	Pitch[1)] *(mm)*	Clearance Drill *(mm)*	Tap Drill *(mm)*	Tensile Stress Area *(mm)*
M 1.6	0.35	1.8	1.25	
M 2	0.40	2.4	1.60	
M 2.5	0.45	2.90	2.00	
M 3	0.50	3.40	2.50	
M 3.5	0.60	3.90	2.90	
M 4	0.70	4.50	3.30	8.78
M 5	**0.80**	5.50	4.20	14.2
M 6	1.00	6.60	5.00	20.1
M 8	1.25	9.00	6.80	36.6
M 10	1.50	12.00	8.50	58.0
M 12	1.75	14.00	10.20	84.3
M 14	2.00	16.00	12.00	
M 16	2.00	18.00	14.00	157
M 20	2.50	22.00	17.50	245
M 22	2.50	25.00	19.50	
M 24	3.00	27.00	21.00	353
M 27	3.00	30.00	24.00	
M 30	3.50	33.00	26.50	561
M 36	4.00	40.00	32.00	817
M 42	4.50	46.00	37.50	1120
M 48	5.00	53.00	43.00	1470
M 56	5.50	62.00	50.50	2030
M 64	6.00	70.00	58.00	2680
M 68	6.00	74.00	62.00	

Table 4. 7 Metric threads - Coarse thread pitches

From the table, we choose M5 coarse thread pitches bolts, with P=0.80 mm, d=5 mm, so its d_1=4.134 mm, which meets the requirement.

4.3 Verification of the vibration oriented mechanism

1. Calculation of the dangerous section area of the bolts

$$A_1 = \frac{\pi {d_1}^2}{4} = 13.42\ mm^2$$

Thus, the dangerous section area A_1 equals to 13.42 mm^2 [46].

2. Calculation of the maximum stress on the bolts

$$\sigma_{max} = \frac{F}{A_1} = 137.06\ N/mm^2$$

Thus, the maximum stress σ_{max} equals to 137.06 N/mm^2.

3. Calculation of the minimum stress on the bolts

$$\sigma_{min} = \frac{F_1}{A_1} = 93.20\ N/mm^2$$

Thus, the maximum stress σ_{min} equals to 93.20 N/mm^2.

4. Calculation of the alternating stress amplitude on the bolts

$$\sigma_a = \frac{\sigma_{max} - \sigma_{min}}{2} = 21.93\ N/mm^2$$

Thus, the alternating stress amplitude σ_a equals to 21.93 N/mm^2.

5. Calculation of the mean stress on the bolts

$$\sigma_m = \frac{\sigma_{max} + \sigma_{min}}{2} = 115.13\ N/mm^2$$

Thus, the alternating stress amplitude σ_m equals to 115.13 N/mm^2.

6. Calculation of other inputs

There are also some inputs should be found: the comprehensive influence coefficient K_σ and the material factor ψ_σ.

6-a. Comprehensive influence coefficient K_σ

There are many factors affecting comprehensive influence coefficient K_σ

Factors related to the component:

- Size, C_S, not considered in tension and compression
- Notches, K_f, the fatigue stress concentration factor

- Surface finishing, C_F
- Surface treatments (mechanical, thermal or chemical, coatings…)

Factors related to service conditions:

- Loading mode, C_L
- Reliability, C_R
- Temperature
- Environment (moisture, corrosives…)

$$K_\sigma = \frac{K_f}{C_L \cdot C_S \cdot C_F \cdot C_R}$$

C_L=0.7 (experimentally 0.6~0.8) for tension/compression

C_F=1, assume surface roughness R_a=0.8.

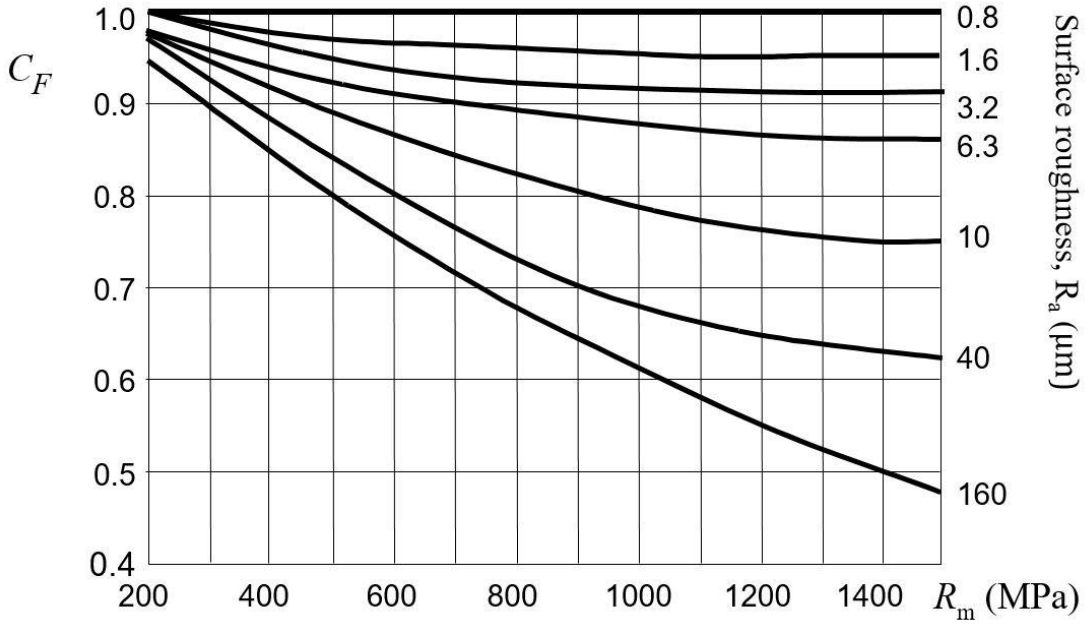

Figure 4. 3 Surface finishing factor

C_R=0.620, assume reliability should be 99.999%.

Reliability	C_R Factor
50%	1.000
90%	0.897
95%	0.868
99%	0.814
99.9%	0.753
99.990%	0.702
99.999%	0.659
99.9999%	0.620
99.99999%	0.584

99.999999%	0.551
99.9999999%	0.520

Table 4. 8 Reliability factor

K_f =1.45, for 1035 steel and M4 bolts with coarse thread pitches.

$$K_\sigma = \frac{K_f}{C_L \cdot C_F \cdot C_R} = 3.341$$

Then we get K_σ equals to 3.341

6-b. Material factor ψ_σ

For carbon steel, the material factor $\psi_\sigma \approx 0.1 \sim 0.2$. For alloy steel, $\psi_\sigma \approx 0.2 \sim 0.3$. As carbon steel in our case, we choose $\psi_\sigma \approx 0.15$.

$$\sigma_{-1} = 0.5R_m = 250\ Mpa$$

For 1035 steel with property class 5.6, its R_m = 500Mpa, so σ_{-1} = 250Mpa.

7. Verification of the fatigue strength

7-a. Verification according to constant minimum stress, σ_{min} = C

For allowable safety factor we choose the maximum value in the range, [n] = 1.5[47]

$$n_a = \frac{2\sigma_{-1} + (K_\sigma - \Psi_\sigma) \cdot \sigma_{min}}{(K_\sigma + \Psi_\sigma) \cdot (2\sigma_a + \sigma_{min})} = 1.72 \geq [n]$$

7-b. Verification according to cyclic alternating stress amplitude

For allowable safety factor we choose the maximum value in the range, allowable safety factor $[n_a]$ = 1.5. For 1035 steel, its effective stress concentration factor k_σ = 3.45.

$$n_\sigma = \frac{[\sigma_a]}{\sigma_a} = \frac{\sigma_{-1}}{[n_a] \cdot k_\sigma \cdot \sigma_a} = 2.20 \geq [n_a]$$

7-c. Verification according to constant stress ratio, r = C

For allowable safety factor we choose the maximum value in the range, [n] = 1.5

$$n_\sigma = \frac{\sigma_{-1}}{K_\sigma \cdot \sigma_a + \Psi_\sigma \cdot \sigma_m} = 2.76 \geq [n]$$

From the above three verification methods, we can find differences among their results but all of them meet the strength condition. Thus, the design that we use M5 coarse thread pitch bolts with 1035 carbon steel property class 5.6 can be verified.

5. Conclusions

Liquid cooling is indeed an effective method to cool down the high power ultra-fast charging system and the application to the market will be a new trend.

From the above research, the preliminary configuration of the cooling system is designed and analyzed, in terms of several important system parameters: the mass flow rate and the heat transfer area. The coolant pipe in this paper merely represents one possible solution, taking into the cooling effectiveness instead of cost and manufacture easiness. Although the specific devices such as radiator, pump and fan are not focused, the simulation process can inclusively consider all elements in this system. In the future, the specific parameters of those devices should be decided.

As for the mechanism part, the fixture method is also designed, with the dimensions of the threaded fasteners, the choice of materials. Although this solution is verified in terms of mechanical performance, the cost and supply are not considered. It is well worthy to note that the formula used for the design are constant and can be used if those parameters changed in the future.

In conclusion, this paper gives a draft design with simplicity, some parts are not fully realistic but consistent with the theoretic knowledge. I hope to refine those aspects in the future.

List of figures

List of tables

Acknowledgements

During the period of my research, I have received great help from my tutor, Professor Guglielmi Paolo, who always answered my question with great patience and precise explanation. With his instruction, I improved my research method significantly, in terms of efficiency and accuracy. Moreover, I also developed great interest in the research field of electrical vehicle. I express my warm appreciation to my professor. Besides, I also got a number of supports from my family, who always encouraged me to continue on my research. In addition, I would like to thank my colleague Xu Haoly, making smooth cooperation with me and we always discussed all perspectives of my research. With their supports, I have had an unforgettable research journey in Politecnico di Torino.

References

[1]. Jaegue Shin, Boyune Song, Seokhwan Lee, Seungyong Shin, Yangsu Kim, Guho Jung, Seongjeub Jeon. "Contactless power transfer systems for On-Line Electric Vehicle (OLEV)", 2012 IEEE International Electric Vehicle Conference, 2012
[2]. "More policies expected to foster growth of green vehicles.", Xinhua News Agency, March 19, 2018 Issue
[3]. Chabaan. "A Comprehensive Review of Wireless Charging Technologies for Electric Vehicles", IEEE Transactions on Transportation Electrification, 2018
[4]. "QCOM, LEA: Hot Stocks.", Theflyonthewall News, July 27, 2016 Issue
[5]. "Qualcomm, Lear Corp. Sign Wireless EV Charging License Agreement.", ICT Monitor Worldwide, July 28, 2016 Issue
[6]. "Qualcomm and Lear sign commercial wireless electric vehicle charging licence agreement.", ICT Monitor Worldwide, July 29, 2016 Issue
[7]. Trivedi, Yatin. "Wireless power transfer: "Look ma, no hands, no wires!"", IEEE Communications Magazine, 2016.
[8]. "Fluid Machinery and Fluid Mechanics", Springer Nature, 2009
[9]. Dinçer. "General Introductory Aspects for Thermal Engineering", Thermal Energy Storage Systems and Applications, 2010
[10]. Akira Masuda, Noriyuki Kimura, Toshimitsu Morizane, Hideki Omori. "Improvement of transmission efficiency on inductive Wireless Power Transfer at a middle distance", 2013 International Conference on Renewable Energy Research and Applications (ICRERA), 2013
[11]. "ABOUT ASSURED", assured-project.eu, May 29, 2017 Issue
[12]. Kaiyuan Deng, Mingzhi He. "Study on thermal design of high-power power supply with synchronous rectifiers", AIP Publishing, 2017
[13]. Zhang, Wei, Jeff C. White, Rajesh K. Malhan, and Chunting Chris Mi. "Loosely Coupled Transformer Coil Design to Minimize EMF Radiation in Concerned Areas", IEEE Transactions on Vehicular Technology, 2016
[14]. Bowen Wu, Jingbiao Liu, Haibin Yu, Zhu Li, Yeming Chen. "Underwater high-power inductive coupling energy transmission system", OCEANS 2016 - Shanghai, 2016
[15]. G. Kreisselmeier. "Adaptive control via adaptive observation and asymptotic feedback matrix synthesis", IEEE Transactions on Automatic Control, 1980
[16]. Zhicong Huang, Siu-Chung Wong, Chi K. Tse. "Control Design for Optimizing Efficiency in Inductive Power Transfer Systems", IEEE Transactions on Power Electronics, 2018
[17]. J. Caldwell, Y. M. Ram. "Mathematical Modelling", Springer Nature, 1999
[18]. Alireza Khaligh. "Stability Criteria for the Energy Storage Bi-directional Dc/Dc Converter in the Toyota Hybrid System II", 2007 IEEE Vehicle Power and Propulsion Conference, 09/2007
[19]. Thiago de Paula Machado Bazzo, Jose Fabio Kolzer, Renato Carlson, Frederic Wurtz,

Laurent Gerbaud. "Multiphysics Design Optimization of a Permanent Magnet Synchronous Generator", IEEE Transactions on Industrial Electronics, 2017

[20]. Yi, Ying, Ulrich Buttner, Yiqiang Fan, and Ian G. Foulds. "Design and optimization of a 3-coil resonance-based wireless power transfer system for biomedical implants: 3-COIL RWPTS FOR BIOMEDICAL IMPLANTS", International Journal of Circuit Theory and Applications, 2014.

[21]. Yasuyuki Shirai, Mariko Mukai, Takuya Sakamoto, Jumpei Baba. "Enhancement Test of Critical Clearing Time of One-Machine Infinite Bus Transmission System by Use of SFCL", IEEE Transactions on Applied Superconductivity, 2018

[22]. Yong Li, Qiaodi Xu, Tianren Lin, Jiefeng Hu, Zhengyou He, Ruikun Mai. "Analysis and Design of Load-Independent Output Current or Output Voltage of a Three-Coil Wireless Power Transfer System", IEEE Transactions on Transportation Electrification, 2018

[23]. Yugang Su, Chunsen Tang, Shuping Wu, Yue Sun. "Research of LCL Resonant Inverter in Wireless Power Transfer System", 2006 International Conference on Power System Technology, 2006

[24]. Jeroen Boeij, Elena Lomonova, Jorge Duarte, Andre Vandenput. "Contactless Energy Transfer to a Moving Load Part II: Simulation of Electrical and Mechanical Transient", 2006 IEEE International Symposium on Industrial Electronics, 2006

[25]. Liang, Chonggan, Longfu Luo, Yong Li, Jiazhu Xu, Qi Qi, Yuehui Chen, Guandong Zhou, and Meihua Deng. "An Integrated Harmonic- Filtering Transformer for Low-Voltage Distribution Systems", IEEE Transactions on Magnetics, 2015

[26]. Schormans, Matthew, Virgilio Valente, and Andreas Demosthenous. "Frequency Splitting Analysis and Compensation Method for Inductive Wireless Powering of Implantable Biosensors", Sensors, 2016.

[27]. Hidekazu Miura. "Synchronous rectification for contactless power supply utilizing Mn–Zn ferrite core coils", Journal of Applied Physics, 2005

[28]. Mariscotti, A., M. Ruscelli, and M. Vanti. "Modeling of Audiofrequency Track Circuits for Validation, Tuning, and Conducted Interference Prediction", IEEE Transactions on Intelligent Transportation Systems, 2010

[29]. Kazimierczuk. "Magnetic Cores", High-Frequency Magnetic Components, 2013

[30]. Byungjoon Yoo, V. Choudhary, T. Mukhopadhyay. "Pricing strategies of electronic B2B marketplaces with two-sided network externalities", Proceedings of the 35th Annual Hawaii International Conference on System Sciences, 2002

[31]. Zhang, Yu, and Jinliang Liu. "Hybrid Energy Storage and Applications Based on High Power Pulse Transformer Charging", Energy Storage - Technologies and Applications, 2013

[32]. Jolita Adamonis, Laura M. Werner. "A NEW MEASURE TO QUANTIFY HYSTERESIS LOSSES: THE CASE OF ITALIAN WINE EXPORTS TO THE UNITED STATES", Macroeconomic Dynamics, 2018

[33]. Kabeya, Kosuke, Shunji Yanase, Yasuo Okazaki, and Kyyoul Yun. "Magnetic Property of Iron-Dust Cores with Mixture of Ferromagnetic Ferrite Powder and Alumina Powder",

IEEE Transactions on Magnetics, 2014

[34]. Cheng, Zhiyuan, Yang Lei, Kai Song, and Chunbo Zhu. "Design and Loss Analysis of Loosely Coupled Transformer for an Underwater High-Power Inductive Power Transfer System", IEEE Transactions on Magnetics, 2015

[35]. Kai Yang. "Thermal behavior analysis of nickel/metal hydride battery during overcharging", Science China Chemistry, 05/2010

[36]. Guangchong FAN, and Zhewei LIN. "Preheating method of lithium-ion batteries in an electric vehicle", Journal of Modern Power Systems and Clean Energy, 2015

[37]. Chunrong Zhao, Wenjiong Cao, Ti Dong, Fangming Jiang. "Thermal behavior study of discharging/charging cylindrical lithium-ion battery module cooled by channeled liquid flow", International Journal of Heat and Mass Transfer, 2018

[38]. Weisong Tian, Yucheng Zhang, Ruiyun Fu, Yanxiao Zhao, Guodong Wang, Robb Winter. "Modeling and control architecture of source and load management in islanded power systems", 2015 IEEE Energy Conversion Congress and Exposition (ECCE), 2015

[39]. Kreith, Frank, Robert Boehm, George Raithby, K Terry Hollands, N Suryanarayana, Thomas Irvine Jr., Massimo Capobianchi, Michael Modest, and Van Carey. "Heat and Mass Transfer", Handbook Series for Mechanical Engineering, 1999

[40]. Yue, An Na, Kun Peng, Ling Ping Zhou, Jia Jun Zhu, and De Yi Li. "Influence of Ti Layer on the Structure and Properties of Al/Cu Thin Film", Advanced Materials Research, 2013

[41]. Engineering ToolBox. Densities of common solids, 2018, https://www.engineeringtoolbox.com/density-solids-d_1265.html

[42]. Jin Wang, Suying Wang, Youtao Zhou. "Study on Ice Storage Characteristics of a Small-scale Storage Tank Filled with Ice Balls", 2010 Asia-Pacific Power and Energy Engineering Conference, 2010

[43]. ISO 898-1:2009(E), Mechanical properties of fasteners made of carbon steel and alloy steel-Part 1: Bolts, screws and studs with specified property classes-Coarse thread and fine pitch thread

[44]. Daining Fang, Faxin Li, Bin Liu, Yihui Zhang, Jiawang Hong, Xianghua Guo. "Advances in Developing Electromechanically Coupled Computational Methods for Piezoelectrics/Ferroelectrics at Multiscale", Applied Mechanics Reviews, 2013

[45]. G.P. Souza, D.A. Oliveira, D.D. Luders, N.M. Kimura, M. Simões, A.J. Palangana. "An analogy between biaxial crystal and biaxial nematic lyotropic phase", Journal of Molecular Liquids, 2010

[46]. Yan, Taoping. "Construction of cylinder head vibration bolts test bench and stress analysis of the bolts", 2012 2nd International Conference on Consumer Electronics Communications and Networks (CECNet), 2012.

[47]. Eike Kiltz, Hans Ulrich Simon. "Threshold circuit lower bounds on cryptographic functions", Journal of Computer and System Sciences, 2005